Monthly Notices
of the
ROYAL ASTRONOMICAL SOCIETY

MNRAS **448,** 135–167 (2015) doi:10.1093/mnras/stu1841

The identification of dust heating mechanisms in nearby galaxies using *Herschel* 160/250 and 250/350 μm surface brightness ratios

G. J. Bendo,[1⋆] M. Baes,[2] S. Bianchi,[3] M. Boquien,[4] A. Boselli,[5] A. Cooray,[6] L. Cortese,[7] I. De Looze,[2] S. di Serego Alighieri,[3] J. Fritz,[2] G. Gentile,[2,8] T. M. Hughes,[2] N. Lu,[9] C. Pappalardo,[10] M. W. L. Smith,[11] L. Spinoglio,[12] S. Viaene[2] and C. Vlahakis[13]

[1] *UK ALMA Regional Centre Node, Jodrell Bank Centre for Astrophysics, School of Physics and Astronomy, University of Manchester, Oxford Road, Manchester M13 9PL, UK*
[2] *Sterrenkundig Observatorium, Universiteit Gent, Krijgslaan 281 S9, B-9000 Gent, Belgium*
[3] *INAF–Osservatorio Astrofisico di Arcetri, Largo Enrico Fermi 5, I-50125 Firenze, Italy*
[4] *Institute of Astronomy, University of Cambridge, Madingley Road, Cambridge CB3 0HA, UK*
[5] *Laboratoire d'Astrophysique de Marseille – LAM, Université d'Aix-Marseille & CNRS, UMR7326, 38 rue F. Joliot-Curie, F-13388 Marseille Cedex 13, France*
[6] *Department of Physics and Astronomy, University of California, Irvine, CA, 92697, USA*
[7] *Centre for Astrophysics & Supercomputing, Swinburne University of Technology, Mail H30, PO Box 218, Hawthorn, VIC 3122, Australia*
[8] *Department of Physics and Astrophysics, Vrije Universiteit Brussels, Pleinlaan 2, B-1050 Brussels, Belgium*
[9] *NASA Herschel Science Center, MS 100-22, California Institute of Technology, Pasadena, CA 91125, USA*
[10] *CAAUL, Observatório Astronómico de Lisboa, Universidade de Lisboa, Tapada da Ajuda, P-1349-018 Lisboa, Portugal*
[11] *School of Physics and Astronomy, Cardiff University, Queens Buildings, The Parade, Cardiff CF24 3AA, UK*
[12] *Istituto di Fisica dello Spazio Interplanetario, INAF, Via del Fosso del Cavaliere 100, I-00133 Roma, Italy*
[13] *Joint ALMA Observatory/European Southern Observatory, Alonso de Cordova 3107, Vitacura, Santiago, Chile*

Accepted 2014 September 4. Received 2014 September 3; in original form 2014 July 25

ABSTRACT

We examined variations in the 160/250 and 250/350 μm surface brightness ratios within 24 nearby (<30 Mpc) face-on spiral galaxies observed with the *Herschel* Space Observatory to identify the heating mechanisms for dust emitting at these wavelengths. The analysis consisted of both qualitative and quantitative comparisons of the 160/250 and 250/350 μm ratios to Hα and 24 μm emission, which trace the light from star-forming regions, and 3.6 μm emission, which traces the light from the older stellar populations of the galaxies. We find broad variations in the heating mechanisms for the dust. In one subset of galaxies, we found evidence that emission at ≤160 μm (and in rare cases potentially at ≤350 μm) originates from dust heated by star-forming regions. In another subset, we found that the emission at ≥250 μm (and sometimes at ≥160 μm) originates from dust heated by the older stellar population. In the rest of the sample, either the results are indeterminate or both of these stellar populations may contribute equally to the global dust heating. The observed variations in dust heating mechanisms do not necessarily match what has been predicted by dust emission and radiative transfer models, which could lead to overestimated dust temperatures, underestimated dust masses, false detections of variability in dust emissivity, and inaccurate star formation rate measurements.

Key words: galaxies: ISM – galaxies: spiral – infrared: galaxies.

1 INTRODUCTION

The *Herschel* Space Observatory (Pilbratt et al. 2010) was the first telescope that had both the sensitivity and spatial resolution to map 250–500 μm dust emission from both compact and diffuse regions within nearby spiral galaxies (galaxies within a distance of 30 Mpc) on spatial scales of the order of 1 kpc. Consequently, the telescope has detected a heretofore unseen dust component in nearby spiral galaxies that is heated primarily by the evolved stellar population and that emits primarily at >250 μm. This component was first identified in M81 by comparing 70/160, 160/250, 250/350, and 350/500 μm surface brightness ratios measured within 0.5 kpc subregions to tracers of star formation and the evolved

⋆ E-mail: george.bendo@manchester.ac.uk

stellar population[1] (Bendo et al. 2010, 2012a). This analysis was more capable than various spectral energy distribution (SED) fitting techniques in detecting this cold component for multiple reasons. First, the analysis utilized the spatial information about both the dust emission and its heating sources. Secondly, it eliminated many assumptions about the SED of the illuminating radiation fields or the physical properties of the dust grains. Thirdly, it made no assumptions about the expected SED shape from the dust emission. Fourthly, it focused on the analysis of subsegments of individual sections of the dust SED rather than attempting to simultaneously describe emission at all wavelengths, which could lead to false assumptions or inferences on the relation between dust seen at shorter and longer wavelengths.

The same methods were later used to detect dust heated by the evolved stellar population in M31 (Planck Collaboration XXV 2014), M33 (Boquien et al. 2011), M83 (Bendo et al. 2012a), and NGC 2403 (Bendo et al. 2012a). In contrast, Galametz et al. (2010) and Hughes et al. (2014) identified nearby galaxies where the infrared surface brightness ratios clearly indicated that dust emission seen at $\leq$350 μm was heated by young stars (generally photoionizing stars $\leq$3 Myr in age) in star-forming regions. Unfortunately, when Boselli et al. (2012) used global infrared surface brightness ratios for spiral galaxies in the *Herschel* Reference Survey (HRS; Boselli et al. 2010), the results were more ambiguous; the ratios were correlated as well with emission from star formation tracers as from the evolved stellar population, probably because stellar mass and star formation rate are correlated when integrated over global scales.

SED fitting techniques have also been used to study dust heating on local and global scales, typically by blindly fitting a model with two or more thermal components [either modified blackbodies or more complex templates that include dust heated locally by star formation and dust heated by the diffuse interstellar radiation field (ISRF)] while ignoring any spatial information on dust heating sources (e.g. Draine et al. 2007; da Cunha, Charlot & Elbaz 2008; Rowan-Robinson et al. 2010; Aniano et al. 2012; Dale et al. 2012; Mentuch Cooper et al. 2012; Ciesla et al. 2014). These approaches may sometimes but not always reproduce the results seen from the analysis of infrared surface brightness ratios. For example, the Draine et al. (2007) dust emission models and the Bendo et al. (2012a) infrared ratio analysis both find for M81 that the 70–500 μm emission is dominated by a component heated by the diffuse ISRF. For NGC 2403, however, the Draine et al. (2007) models predict that dust heated by the diffuse ISRF is seen at $>$70 μm, whereas the Bendo et al. (2012a) analysis found that dust heated locally by star-forming regions dominates the SED at $<$160 μm. This example demonstrated that, while these dust models may accurately replicate the magnitudes of the observed infrared surface brightnesses of extragalactic sources, it is unclear that they can replicate the infrared colours of these sources, which may indicate deeper problems with how the dust absorption and emission are modelled as well as how the dust mass is estimated.

[1] Bendo et al. (2012a) refer to this as the 'total stellar population', as they did not remove the contribution of younger stars to the near-infrared band used to trace this population. We explicitly demonstrate that photoionizing stars have a minimal effect on the near-infrared data we use, but non-photoionizing intermediate-aged stars with ages $<$100 Myr may still strongly influence the near-infrared bands. For simplicity, we refer to this as the 'evolved stellar population' in this paper.

Radiative transfer models that reproduce the dust attenuation in ultraviolet and optical wavelengths as well as the emission at infrared wavelengths (e.g. Silva et al. 1998; Misiriotis et al. 2001; Bianchi 2008; Baes et al. 2011; Popescu et al. 2011; Domínguez-Tenreiro et al. 2014) can also be used to examine dust heating. These models can quantify dust heating by different stellar populations and can also account for the propagation of radiation through the interstellar medium (ISM), which allows them to characterize non-local dust heating. However, such models are generally more easily applied to edge-on galaxies where structures are integrated along the line of sight and information about the spatial distribution of stars and dust is lost, although De Looze et al. (2014) have performed radiative transfer modelling of the face-on spiral galaxy M51. The models are also heavily dependent upon properly characterizing both the stellar populations and the dust properties, whereas more empirically based analyses relating colour variations to dust heating sources are not strongly affected these issues.

It is also common to estimate dust temperatures and masses by fitting all far-infrared data at $\geq$100 or $\geq$160 μm using a single blackbody modified by an emissivity law that scales as $\lambda^{-\beta}$ (e.g. Smith et al. 2010, 2012b; Davies et al. 2012; Foyle et al. 2012; Galametz et al. 2012; Groves et al. 2012; Auld et al. 2013; Cortese et al. 2014; Tabatabaei et al. 2014). This often relies upon the a priori assumption that all emission seen within a wavelength range in all locations in all galaxies can be attributed to a single thermal component with a single heating source. However, as can be seen from the results from Bendo et al. (2012a), the wavelength at which the SED transitions between dust heated by the ISRF and dust heated by star-forming regions may be different for different galaxies. In some cases, the transition occurs between 160 and 250 μm (as seen in M33, M83 and NGC 2403), while in other cases, the transition may occur at $<$160 μm (as seen in the outer disc of M81), and in some locations, it is possible to see dust emission over the 70–500 μm range heated by a single thermal component (as seen in the centre of M81).

Hence, while single thermal component fits to 100–500 μm data may accurately describe the shape of the galaxy SEDs, the dust temperatures and masses as well as dust emissivity variations implied by the fits may not represent the true physical properties of the coldest dust within the galaxies. Furthermore, measured dust emissivity variations among or within galaxies may actually be indicative of issues with properly separating emission from warmer and colder dust components (e.g. Kirkpatrick et al. 2014). Moreover, Galliano et al. (2011) and Xilouris et al. (2012) have demonstrated that colder diffuse dust could effectively be masked by warmer components in SED fits unless special care was taken to spatially separate the components.

It is critically important to properly identify the heating sources for dust in galaxies and to properly separate dust into individual thermal components with different heating sources so that the temperature of the colder dust can be determined accurately. Since the colder thermal component typically contains most of the dust mass, the accuracy of the colder dust temperature has an effect on the accuracy of dust mass measurements. Accurate dust temperature and mass measurements may be critically important if dust mass is used as a proxy for gas mass in scenarios where emission from gas cannot be directly measured or in studies where estimates of the gas mass may be uncertain, such as when the conversion from CO line emission to molecular gas mass is suspect.

It is also important to identify the heating sources of dust so as to accurately model radiative transfer within galaxies. Moreover, it is possible that far-infrared emission is related to star formation not

because the dust is heated by young stars but instead because the dust traces the gas fuelling star formation, as suggested by Boquien et al. (2011) and Bendo et al. (2012a). If so, then this could affect how star formation is calculated using far-infrared flux measurements and could also affect the analyses of things such as gas-depletion times in normal and starburst galaxies, the far-infrared-to-radio correlation, and the 'main-sequence' relation between star formation rate and stellar mass.

To better understand dust heating mechanisms within nearby galaxies, we present here an expanded comparison of infrared surface brightness ratios to dust heating sources within a set of 24 face-on spiral galaxies with well-resolved far-infrared emission that consists of 11 galaxies from the HRS, 10 galaxies from the Key Insights on Nearby Galaxies: A Far-Infrared Survey with *Herschel* (KINGFISH; Kennicutt et al. 2011), and the three galaxies from Bendo et al. (2012a). This larger sample of galaxies can be used to determine whether the cold dust component heated by the evolved stellar population is consistently seen among all spiral galaxies or if, in some spiral galaxies, star formation may be the dominant heating source for the dust seen at all wavelengths. Additionally, with the larger sample of galaxies, it will be possible to look at variations in the relative contributions of star-forming regions and the evolved stellar populations among a large sample of galaxies [as already seen within the three galaxies studied by Bendo et al. (2012a)] and to possibly link these variations with other physical properties of the galaxies.

The analysis primarily focuses on the 160/250 and 250/350 μm surface brightness ratios based on 160 μm data taken with the Photodetector Array Camera and Spectrometer (PACS; Poglitsch et al. 2010) and 250 and 350 μm data taken with the Spectral and Photometric Imaging REceiver (SPIRE; Griffin et al. 2010). These data cover the transition between warmer dust heated by star-forming regions and colder dust heated by the evolved stellar population found previously by Bendo et al. (2010, 2012a) and Boquien et al. (2011), so this is a good part of the far-infrared waveband to examine. We had PACS 70 and 100 μm data for most galaxies in our sample but did not use it in most of our analysis because we had difficulty detecting emission above a 3σ threshold from diffuse low surface brightness regions, particularly in the outer parts of the optical discs. SPIRE 500 μm data were also available, but we did not use the data mainly because the 500 μm point spread function (PSF) has a full width at half-maximum (FWHM) of 36 arcsec, which would cause problems with attempting to resolve structures within many of the sample galaxies. Moreover, although Bendo et al. (2012a) was still able to relate the 350/500 μm variations in their galaxies to heating sources, it was clear that the 350/500 μm ratios were relatively insensitive to temperature variations compared to shorter wavelength ratios. For these reasons, we limit our analyses to the 160/250 and 250/350 μm ratios.

Following descriptions of the sample in Section 2 and the data in Section 3, we present three different parts of the analysis. Section 4 presents a qualitative analysis in which we compare 160/250 and 250/350 μm surface brightness ratio maps to tracers of star-forming regions and the evolved stellar population. Section 5 presents a quantitative comparison of the 160/250 and 250/350 μm ratios to the tracers of these two different heating sources. Section 6 includes an analytical approach first proposed by Bendo et al. (2012a) in which the 160/250 and 250/350 μm ratios are fitted as a function of both the evolved stellar population and star formation; the results of the fits can be used to determine the fraction of the variation in the surface brightness ratios that can be attributed to a dust heating source. After this analysis, we discuss the implications of the results for modelling dust emission and for measuring star formation rates in Section 7. A summary of our results for each galaxy as well as for the sample as a whole is presented in Section 8.

2 SAMPLE

As stated in the introduction, the sample used for this analysis is drawn from three other samples: HRS, KINGFISH, and the Bendo et al. (2012a) sample, which is a subsample of galaxies from the Very Nearby Galaxies Survey (VNGS; PI: C. Wilson). The three surveys have different purposes. The HRS is a complete sample of 323 galaxies that fall within distances between 15 and 25 Mpc that are also brighter than *K*-band total magnitude of 12 (applied to Sa-Im and blue compact dwarf galaxies) or 8.7 (applied to E, S0, and S0/a galaxies). This survey is intended to provide statistical information about the properties of galaxies (e.g. far-infrared colours, far-infrared luminosities, dust temperatures, dust masses, dust emissivities, etc.). KINGFISH is a continuation of the *Spitzer* Infrared Nearby Galaxies Survey (SINGS; Kennicutt et al. 2003) and consists of a sample of galaxies selected to span a range of morphologies, infrared luminosities, and infrared/optical luminosity ratios. The sample does not have the same applications as a volume- or flux-limited sample, but since SINGS and KINGFISH have also gathered additional infrared spectral data and other ancillary data for the galaxies, the sample is very useful for multiwavelength analyses. The VNGS is a project that observed 13 galaxies with *Herschel*, and while the sample is not a statistically complete or representative sample, it includes many very well-studied nearby galaxies, many of which are archetypal representatives of a class of objects (e.g. Arp 220, Cen A, M82).

Using data from all three of these surveys is not ideal, as the resulting sample is somewhat heterogeneous. However, given the stringent selection criteria that we needed to apply, it was necessary to select galaxies from multiple surveys to build up our sample. The HRS and KINGFISH samples were used mainly because they are two of the largest photometric surveys performed with *Herschel* that included spiral galaxies. The VNGS galaxies were included mainly because the data from the previous analysis are already in hand.

To select galaxies for our analysis, we applied the following criteria.

(1) The galaxies must have morphological types between Sa and Sd. Irregular galaxies have low infrared surface brightnesses, making it difficult for us to apply our analysis methods. Emission from E-S0/a galaxies is generally compact (e.g. Bendo et al. 2007; Muñoz-Mateos et al. 2009; Smith et al. 2012a), so the infrared emission observed by *Herschel* is usually unresolved or marginally resolved, and our analysis will not work. In the cases where emission is detected in extended structures in E-S0/a galaxies (such as NGC 1291 or NGC 4406), it is impractical to work with the data because of the relatively low surface brightness of the extended emission.

(2) The galaxies must be face-on (with minor/major axis ratios of >0.5). This eliminates edge-on and steeply inclined galaxies where integration along the line of sight may complicate the analysis.

(3) The galaxies must have optical major axes that are >5 arcmin. This ensures that sufficient data are available to examine substructures within the galaxies at the resolution of the 350 μm data.

(4) After the application of the data preparation steps in Section 3.4, the 250/350 μm surface brightness ratio must be measured at the 3σ level within a ≥ 7 arcmin^2 area (which is equivalent to the area of a circle with a diameter of ≥ 3 arcmin). This ensures

Table 1. Sample galaxies.

Galaxy	Survey[a]	Hubble type[b]	Size of optical disc (arcmin[b])	Distance (Mpc)	Distance reference	Physical size of 24 arcsec (kpc)
NGC 628 (M74)	KINGFISH	SA(s)c	10.5 × 9.5	9.9 ± 1.2	Olivares et al. (2010)	1.2
NGC 925	KINGFISH	SAB(s)d	10.4 × 5.8	9.2 ± 0.2	Freedman et al. (2001)	1.1
NGC 2403	VNGS	SAB(s)cd	21.9 × 12.3	3.2 ± 0.4	Freedman et al. (2001)	0.4
NGC 3031 (M81)	VNGS	SA(s)ab	26.9 × 14.1	3.6 ± 0.1	Freedman et al. (2001)	0.4
NGC 3184	KINGFISH	SAB(rs)cd	7.4 × 6.9	12.6 ± 1.6	Olivares et al. (2010)	1.5
NGC 3621	KINGFISH	SA(s)d	12.3 × 7.1	6.6 ± 0.2	Freedman et al. (2001)	0.8
NGC 3631	HRS	SA(s)c	5.0 × 3.2	17.5 ± 3.2	Thereau et al. (2007)	2.0
NGC 3938	KINGFISH	SA(s)c	5.3 × 4.9	17.9 ± 1.1	Poznanski et al. (2009)	2.1
NGC 3953	HRS	SB(r)bc	6.9 × 3.5	17.5 ± 0.8	Dessart et al. (2008)	2.0
NGC 4254 (M99)	HeViCS/HRS/KINGFISH	SA(s)c	5.3 × 4.6	14.6 ± 1.9	Poznanski et al. (2009)	1.7
NGC 4303 (M61)	HeViCS/HRS	SAB(rs)bc	6.4 × 5.7	12.2 ± 1.9	Roy et al. (2011)	1.4
NGC 4321 (M100)	HeViCS/HRS/KINGFISH	SAB(s)bc	7.4 × 6.3	15.2 ± 0.5	Freedman et al. (2001)	1.8
NGC 4501 (M88)	HeViCS/HRS	SA(rs)b	6.9 × 3.7	11.7 ± 1.4	Amanullah et al. (2010)	1.4
NGC 4535	HeViCS/HRS	SAB(s)c	7.1 × 5.0	15.8 ± 3.6	Freedman et al. (2001)	1.8
NGC 4548 (M91)	HeViCS/HRS	SB(rs)b	5.4 × 4.3	16.2 ± 0.4	Freedman et al. (2001)	1.9
NGC 4579 (M58)	HeViCS/HRS/KINGFISH	SAB(rs)b	5.9 × 4.9	18.8 ± 3.0	Tully et al. (2009)	2.2
NGC 4725	HRS/KINGFISH	SAB(r)ab pec	10.7 × 7.6	12.4 ± 0.3	Freedman et al. (2001)	1.4
NGC 4736 (M94)	KINGFISH	RSA(r)ab	11.2 × 9.1	5.2 ± 0.4	Tonry et al. (2001)	0.6
NGC 5055 (M63)	KINGFISH	SA(rs)bc	12.6 × 7.2	7.9 ± 1.3	Tully et al. (2009)	0.9
NGC 5236 (M83)	VNGS	SAB(s)c	12.9 × 11.5	4.6 ± 0.3	Saha et al. (2006)	0.5
NGC 5364	HRS	SA(rs)bc pec	6.8 × 4.4	21.6 ± 4.0	Thereau et al. (2007)	2.5
NGC 5457 (M101)	KINGFISH	SAB(rs)cd	28.8 × 26.9	6.7 ± 0.3	Freedman et al. (2001)	0.8
NGC 6946	KINGFISH	SAB(rs)cd	11.5 × 9.8	4.7 ± 0.7	Olivares et al. (2010)	0.5
NGC 7793	KINGFISH	SA(s)d	9.3 × 6.3	3.4 ± 0.1	Pietrzynski et al. (2010)	0.4

Note: [a]The surveys that include the galaxy in this list. In some cases, galaxies appear in multiple surveys.
[b]Data are taken from de Vaucouleurs et al. (1991).

that enough data from each galaxy are available for the analysis. (The HRS galaxies NGC 3227, 3338, and 4450 and the KINGFISH galaxies NGC 1512 and 4826 satisfy criteria 1–3 but not criterion 4.)

(5) The galaxies should not contain infrared-bright point-like nuclei that contain significant fractions ($\gtrsim$30 per cent) of the total infrared flux. This is partly because the PSF matching steps we apply in Section 3.4 produce severe artefacts in the ratio maps around such bright sources; excluding the artefacts also results in excluding large fractions of the infrared emission from the galaxies. High contrast between the central region and the rest of the disc also produces ambiguous results when comparing infrared surface brightness ratios to emission from multiple dust heating sources. This criterion excludes NGC 1097 and 3351 from the sample.

A total of 24 galaxies meet all five of the above criteria. The sample galaxies along with the survey from which the data were taken and morphological, optical disc, and distance information are listed (with the galaxies sorted by the NGC number) in Table 1. Seven of the HRS galaxies fall within the ∼64 deg^2 fields mapped by the *Herschel* Virgo Cluster Survey (HeViCS; Davies et al. 2010) at 100–500 μm; we used the HeViCS data for some of these targets. We also note that four galaxies fall within both the HRS and KINGFISH surveys.

3 DATA

3.1 Far-infrared data

As stated in Section 1, the analysis mainly relies upon 160 μm data acquired with PACS and 250 and 350 μm data acquired with SPIRE. However, we did reprocess the PACS 100 μm images of NGC 628 and 5457 for performing global photometry measurements on those two galaxies (see Section 7.1). The PACS and SPIRE data were obtained by the surveys specified in Table 1. We used the HeViCS parallel-mode scan map data (which simultaneously produced PACS and SPIRE data) to create the 160 μm image of NGC 4254 and the 160–350 μm images of NGC 4303 and 4535. For all other galaxies, we used standard PACS and SPIRE scan map data. Details on the observations are given by Bendo et al. (2012a) for the VNGS galaxies, Auld et al. (2013) for HeViCS, Boselli et al. (2010) and Cortese et al. (2014) for HRS galaxies not in the HeViCS fields, and Kennicutt et al. (2011) for KINGFISH galaxies not in the HRS sample.

The individual PACS data frames were all uniformly reprocessed using the standard PACS pipeline within the *Herschel* Interactive Processing Environment (HIPE; Ott 2010) version 12.0, which includes cosmic ray removal and crosstalk correction. The data were then mosaicked using SCANAMORPHOS version 23 (Roussel 2013), which also removes variations in the instrumental background signal over time. The final pixel scales are 1.7 arcsec at 100 μm and 2.85 arcsec and 160 μm. We then applied colour correction factors of 1.03 ± 0.06 to the 100 μm data and 1.01 ± 0.07 to the 160 μm data based on what would be expected for emission from a modified blackbody with a temperature between 15 and 40 K and a β value between 1 and 2 (Müller et al. 2011)[2]. The FWHM of the PSF is approximately 7 arcsec at 100 μm and 12 arcsec at 160 μm (Lutz 2012)[3]. The flux calibration uncertainty is 5 per cent (Altieri & Vavrek 2013),[4] and along with the colour correction, the overall uncertainties in the scaling of the flux densities is ∼9 per cent.

[2] http://herschel.esac.esa.int/twiki/pub/Public/PacsCalibrationWeb/cc_report_v1.pdf
[3] https://herschel.esac.esa.int/twiki/pub/Public/PacsCalibrationWeb/bolopsf_20.pdf
[4] http://herschel.esac.esa.int/Docs/PACS/pdf/pacs_om.pdf

The SPIRE data were all uniformly reprocessed using HIPE developer build version 12.0. The timeline data were processed through the standard pipeline, which includes electrical crosstalk correction, cosmic ray removal, signal jump removal, and response corrections. In place of the temperature drift removal and baseline signal removal, however, we used the Bright Galaxy Adaptive Element method (Smith 2012; Auld et al. 2013; Smith et al., in preparation), which uses the SPIRE thermistors to characterize the drift in the background signal. Relative gain corrections were applied to correct for the responsivities of the bolometers to extended sources. The data were then mapped using the naive mapmaker within HIPE using final pixel scales of 6 arcsec at 250 μm and 8 arcsec and 350 μm. To optimize the data for extended source photometry, we applied the $K_{\rm PtoE}$ values of 91.289 and 51.799 MJy sr^{-1} (Jy beam^{-1})$^{-1}$ as suggested by the SPIRE Handbook Version 2.5 (Valtchanov 2014)[5]. We also applied colour corrections of 0.997 ± 0.029 to the 250 μm data and 0.991 ± 0.030 to the 350 μm data, which should be appropriate for extended modified blackbody emission with temperatures between 10 and 40 K and β of 1.5 or 2 (Valtchanov 2014). The FWHM is approximately 18 arcsec at 250 μm and 25 arcsec at 350 μm (Valtchanov 2014). The overall uncertainties in the scaling of the flux densities, which encompass the uncertainties from the flux calibration from Bendo et al. (2013), the correction factors for the older flux calibration, the beam area uncertainties, and the colour correction uncertainties, are ∼5 per cent.

Note that the uncertainties in the flux densities and the correction factors applied to the data do not generally affect most of analysis, which is dependent upon the relative variations in surface brightness ratios and therefore independent of the exact scale of the surface brightnesses. The only part of the analysis that is significantly affected is the analysis on the SEDs in Section 7.1, where the absolute values affect the resulting dust masses and temperatures.

3.2 Star formation tracers

To trace the energy from star-forming regions that is heating the dust, we have a few options. Ultraviolet, Hα, and mid-infrared (22 or 24 μm) images are available for most or all of the sample galaxies. However, these three star formation tracers have different strengths and weaknesses.

Uniform ultraviolet images from the *Galaxy Evolution Explorer* are available for 22 of the galaxies, but the emission is very strongly affected by dust extinction. Also, while Hα and 24 μm emission tend to trace O stars with <3 Myr lifespans, ultraviolet light can trace B and A stars with lifespans of tens of Myr. Consequently, ultraviolet emission traces different structures than Hα or 24 μm emission (e.g. Calzetti et al. 2005). Given these complications, we did not work with ultraviolet data for our analysis.

Hα images are very useful to work with because they trace not only emission from photoionized gas within star-forming regions themselves but also the photoionizing light from the star-forming regions that is absorbed by the diffuse ISM. If the diffuse dust outside star-forming regions is partially heated by these photons, then we should find a better correlation between the far-infrared colours and Hα emission. Additionally, the Hα band will be relatively unaffected by older stellar populations since stars with ages of <3 Myr produce relatively few photoionizing photons [as can be seen, for example, in the simulations from Leitherer et al. (1999)]. Hα light is affected by dust extinction, but most star-forming regions are still visible in optical light; only ∼4 per cent of all star-forming regions are completely obscured in the Hα band (Prescott et al. 2007). Although Hα is theoretically a good star formation tracer, the Hα images available for our analysis are sometimes difficult to deal with in practice. The data were acquired from multiple telescopes, have multiple pixel scales and PSF sizes, and cover varying amounts of area around the targets. Moreover, because Hα images are produced by subtracting continuum emission from the data, the images often contain artefacts such as residual background structures or incompletely subtracted starlight from either foreground stars or the bulge stars within the target galaxies. Furthermore, Hα images often contain additional [N II] emission that cannot be easily removed on a pixel-by-pixel basis.

Mid-infrared hot dust emission as observed at 24 μm by the Multiband Imaging Photometer for *Spitzer* (MIPS; Rieke et al. 2004) on the *Spitzer* Space Telescope (Werner et al. 2004) or at 22 μm by the *Wide-field Infrared Survey Explorer* (*WISE*; Wright et al. 2010) is available for all of the galaxies in the sample. Mid-infrared bands are as effective as hydrogen recombination lines in measuring star formation within compact sources (e.g. Calzetti et al. 2005, 2007; Prescott et al. 2007), and the emission is unaffected by dust extinction except in extreme environments. However, the band may also include emission from diffuse dust heated by older stars (e.g. Kennicutt et al. 2009). The mid-infrared data are relatively straightforward to work with in practice. While the data from the two telescopes differ in format, the images from each telescope all have a uniform format, even though the *Spitzer* data may have been processed by different groups using slightly different data reduction pipelines.

Several authors have also published equations in which a tracer of unobscured star formation and a tracer of obscured star formation are combined together to produce a more robust star formation tracer. We decided to use a combined Hα and mid-infrared (22 or 24 μm) metric for most of our analysis because both trace very similar structures (Calzetti et al. 2007), which means that they trace regions affected by the same populations of photoionizing stars. For combining Hα emission with mid-infrared emission, we used

$$f(\mathrm{H}\alpha)_{\rm corrected} = f(\mathrm{H}\alpha)_{\rm observed} + 0.020\nu f_{\nu}(24\,\mu\mathrm{m}) \quad (1)$$

from Kennicutt et al. (2009), which we will henceforth refer to as the extinction-corrected Hα emission. We decided to use this relation because it was derived to work with emission from both compact and diffuse emission [as opposed to the calibration derived by Calzetti et al. (2007), which is better suited for compact regions after the application of local background subtraction]. We lack *Spitzer* 24 μm data for NGC 3631 and NGC 5364 and used *WISE* data as a substitute (although, when we refer to the *Spitzer* and *WISE* data together, we will use the term 24 μm data for simplicity). Although separate calibrations have been derived for combining Hα and *WISE* data by Lee, Hwang & Ko (2013), the coefficients in the equivalent equation differ by a factor of 1.5 from the coefficients for *Spitzer* 24 μm data by Kennicutt et al. (2009) or other authors (e.g. Zhu et al. 2008) even though the *Spitzer* 24 μm and *WISE* 22 μm flux densities do not differ this much. Hence, we also use equation (1) for the *WISE* data. We did not have access to suitable Hα data for NGC 4736 or 6946 that cover the full optical discs of these galaxies, so we used the *Spitzer* 24 μm data by itself as a star formation tracer for these galaxies.

The combined Hα and mid-infrared metric is still not a perfect star formation tracer, mainly because it still potentially includes diffuse 24 μm emission heated by the ISRF from older stars. It is also possible that the dust heated by star-forming regions may

[5] http://herschel.esac.esa.int/Docs/SPIRE/spire_handbook.pdf

Table 2. Information on Hα data.

Galaxy	Hα Source	PSF FWHM (arcsec)	Pixel size (arcsec)	1σ sensitivity (10^{-17} erg cm^{-2} s^{-1} arcsec^{-2})[a]	Calibration uncertainty	Foreground extinction[b]	[N II]/Hα ratio	[N II]/Hα reference[c]
NGC 628	SINGS	2	0.43	0.9	10 per cent	0.152	0[d]	
NGC 925	Boselli & Gavazzi (2002)	5	0.69	4.5	5 per cent	0.165	0.20	K09
NGC 2403	Boselli & Gavazzi (2002)	3	0.69	2.1	5 per cent	0.087	0.22	K09
NGC 3031	Boselli & Gavazzi (2002)	3	0.69	5.6	5 per cent	0.174	0.55	K09
NGC 3184	SINGS	2	0.30	3.7	10 per cent	0.036	0.52	K09
NGC 3621	SINGS[e]	1	0.27	27.9	10 per cent	0.046	0.40	K09
NGC 3631	Boselli et al. (in preparation)	2	0.31	6.8	5 per cent	0.036	0.11	B13
NGC 3938	SINGS	2	0.30	1.4	10 per cent	0.046	0.42	K09
NGC 3953	Boselli et al. (in preparation)	2	0.31	2.3	5 per cent	0.065	0.52	B13
NGC 4254	Boselli & Gavazzi (2002)	3	0.69	1.9	5 per cent	0.084	0.42	B13
NGC 4303	Boselli & Gavazzi (2002)	2	0.41	2.5	5 per cent	0.048	0.48	B13
NGC 4321	Boselli & Gavazzi (2002)	3	0.69	1.7	5 per cent	0.057	0.48	B13
NGC 4501	Boselli & Gavazzi (2002)	3	0.69	2.0	5 per cent	0.082	0.47	B13
NGC 4535	Boselli & Gavazzi (2002)	3	0.69	2.8	5 per cent	0.042	0.49	B13
NGC 4548	Boselli et al. (in preparation)	2	0.41	1.3	5 per cent	0.083	0.41	B13
NGC 4579	Boselli et al. (in preparation)	2	0.41	6.3	5 per cent	0.088	0.92	B13
NGC 4725	SINGS	2	0.31	1.6	10 per cent	0.026	0.49[g]	
NGC 4736	[f]							
NGC 5055	SINGS[e]	2	0.38	6.9	10 per cent	0.038	0.49	K09
NGC 5236	Meurer et al. (2006)	2	0.43	5.3	4 per cent	0.144	0.40[h]	K08
NGC 5364	Boselli et al. (in preparation)	2	0.31	5.3	5 per cent	0.059	0.46[g]	
NGC 5457	Hoopes, Walterbos & Bothun (2001)[e]	6	2.03	0.7	15 per cent	0.019	0.54	K08
NGC 6946	[f]							
NGC 7793	SINGS	1	0.43	2.6	10 per cent	0.042	0[d]	

Note: [a]These 1σ sensitivities correspond to measurements in the original data (before any convolution or rebinning steps are applied). It does include corrections that remove foreground extinction and emission from the [N II] line.
[b]The foreground extinction is based on the *R*-band values calculated by NED using the results from Schlafly & Finkbeiner (2011).
[c]The following abbreviations correspond to the following references: B13: Boselli et al. (2013); K08: Kennicutt et al. (2008); K09: Kennicutt et al. (2009).
[d]The Hα filter used in these observations did not include any [N II] emission, so no correction was needed.
[e]Not enough information was provided with these Hα image files to allow us to convert the data to intensity units, so we rescaled the integrated signal within the optical discs of these galaxies using Hα fluxes from the literature. The correction for [N II] emission was applied during this step.
[f]The Hα data available for these galaxies were not suitable for analysis. See Section 3.2 for details.
[g]We were unable to find any references with data on the [N II]/Hα ratios for these galaxies, so we instead estimated the ratio using the relation between the [N II]/Hα ratio and *B*-band emission given by Kennicutt et al. (2008). We used *B*-band absolute magnitudes of -20.77 for NGC 4725 (based on the photometry from Dale et al. 2007) and -20.60 for NGC 5364 (based on the photometry from de Vaucouleurs et al. 1991). Both absolute magnitudes were calculated using the distances given in Table 1 and include foreground extinction corrections calculated by NED using the results from Schlafly & Finkbeiner (2011).
[h]The filters used for these Hα observations only included emission from the 6584 Å line, so we adjusted the [N II]/Hα ratio by 0.75 based on the spectroscopy data from Storey & Zeippen (2000).

correlate better with one of the star formation tracers instead of the other. Hence, in Appendix A, we examined how using Hα or 24 μm emission by themselves affected the results for the quantitative analysis in Section 5. We found seven galaxies where using one tracer instead of the other could have a significant impact on identifying the dust heating sources, but for most galaxies, the results do not depend upon the selected star formation tracer. It is also possible that other star formation tracers could be better related to the infrared surface brightness variations because they more accurately trace the population that is heating the dust, but it was beyond the scope of this paper to investigate tracers other than Hα and 24 μm emission.

Table 2 lists the sources of the Hα data that we used in this analysis as well as some of the characteristics of the data and corrections applied to the data. We generally gave preference to data that covered the entire target and where the background was close to flat. For NGC 3621 and 3938, we use images that have not been converted into physical units (e.g. erg cm^{-2} s^{-1}) and that we could not determine how to convert into physical units using the available reference information for the images. We therefore rescaled the total fluxes within the optical disc of each galaxy using the global Hα fluxes from Kennicutt et al. (2009). The image of NGC 5457 from Hoopes et al. (2001) was rescaled in a similar way using the photometry published within that paper. For all images, we also applied a foreground extinction correction based on the *R*-band extinction calculated by the NASA/IPAC Extragalactic Database (NED) using the results from Schlafly & Finkbeiner (2011). These corrections change the Hα emission by <10 per cent. Many but not all of the Hα images include emission from one or both [N II] lines at 6548 and 6583 Å. We include corrections for these lines based on [N II]/Hα ratios from several references in the literature. Since the ratios are either global or nuclear measurements, we are only able to use these ratios to uniformly rescale the Hα emission, although the ratio may vary within the galaxies.

Table 3 lists the sources of the 24 μm data used in the analysis. For VNGS and HRS galaxies, we used the *Spitzer* 24 μm images from Bendo, Galliano & Madden (2012b) except for NGC 3631 and NGC 5364, where we used the *WISE* 22 μm images. For the KINGFISH galaxies, we used the SINGS images from Dale et al. (2007) except in the case of NGC 5457, where we used the *Spitzer*

Table 3. Sources of mid-infrared data.

Galaxy	Data source	
	3.6 μm	24 μm
NGC 628	SINGS	SINGS
NGC 925	SINGS	SINGS
NGC 2403	SINGS	Bendo et al. (2012b)
NGC 3031	SINGS	Bendo et al. (2012b)
NGC 3184	SINGS	SINGS
NGC 3621	SINGS	SINGS
NGC 3631	S^{4}G	*WISE*[a]
NGC 3938	SINGS	SINGS
NGC 3953	S^{4}G	Bendo et al. (2012b)
NGC 4254	SINGS	Bendo et al. (2012b)
NGC 4303	S^{4}G	Bendo et al. (2012b)
NGC 4321	SINGS	Bendo et al. (2012b)
NGC 4501	S^{4}G	Bendo et al. (2012b)
NGC 4535	S^{4}G	Bendo et al. (2012b)
NGC 4548	S^{4}G	Bendo et al. (2012b)
NGC 4579	SINGS	Bendo et al. (2012b)
NGC 4725	SINGS	Bendo et al. (2012b)
NGC 4736	SINGS	SINGS
NGC 5055	SINGS	SINGS
NGC 5236	LVL	Bendo et al. (2012b)
NGC 5364	S^{4}G	*WISE*[a]
NGC 5457	LVL	LVL
NGC 6946	SINGS	SINGS
NGC 7793	SINGS	SINGS

Note: [a]*Spitzer* 24 μm data were not available for these galaxies. We used *WISE* 22 μm data as a substitute.

Local Volume Legacy (LVL) Survey data from Dale et al. (2009). All MIPS 24 μm data have plate scales of 1.5 arcsec, PSF FWHM of 6 arcsec (Engelbracht et al. 2007), and calibration uncertainties of 4 per cent (Engelbracht et al. 2007). The *WISE* data are taken from the All-Sky Data Release (2012 March 14) and have plate scales of 1.375 arcsec, PSF FWHM of 12 arcsec (Wright et al. 2010), and calibration uncertainties of 3 per cent (Cutri et al. 2013)[6]. We examined the effects of applying a correction, such as the one given by Helou et al. (2004), to remove the stellar continuum emission within the 24 μm band, but we found that this is not necessary for our analysis. Typically, <5 per cent of the emission in the 24 μm band is from the stellar population seen at 3.6 μm, so applying the correction has a <1 per cent effect on the logarithm of the 24 μm surface brightness and therefore does not have a significant effect on our overall results. We discuss this further in Appendix B.

3.3 Stellar population tracers

Near-infrared bands sample the Rayleigh–Jeans side of the starlight SED and therefore trace the evolved stellar populations very effectively. We have access to uniformly processed Two-Micron All-Sky Survey (2MASS) *J*-, *H*-, and *K*-band data from Jarrett et al. (2003). We also have *Spitzer* 3.6 μm data for all of the sample galaxies, and while the data were processed by several different groups, the groups used similar processing pipelines to produce images with a uniform format. From a physical standpoint, each band has different advantages and disadvantages. The shorter bands are more affected by dust extinction, while the 3.6 μm band may sometimes include thermal emission from dust or polycyclic aromatic hydrocarbons (PAH; Lu et al. 2003; Mentuch et al. 2009; Mentuch, Abraham & Zibetti 2010), although the contribution of these sources of emission to the 3.6 μm band may be $\lesssim$10 per cent (e.g. Meidt et al. 2012). Technically, the 3.6 μm data are better than the 2MASS data. The 3.6 μm data have a smaller PSF, which aids in detecting and removing foreground stars, and the signal-to-noise ratios are much higher in the 3.6 μm data.

Hence, we opted to use the 3.6 μm data as a tracer of the evolved stellar populations in our analysis because of its better data quality. However, we did examine the relation between *H*-band and 3.6 μm data for our sample galaxies to demonstrate that the selection of the band has a negligible impact on the overall analysis. This is shown in Appendix C. We also investigated the possibility of using the extinction-corrected Hα emission to remove the contribution of the star-forming regions to the 3.6 μm band, which would make the band a more effective tracer of intermediate-aged and evolved stars. When we applied such a correction to the 3.6 μm band, we found that it has an effect of $\lesssim$2 per cent for most regions within the sample galaxies. This is equivalent to a change of <1 per cent in the logarithm of the 3.6 μm surface brightness, so we decided not to apply such corrections. This is discussed further in Appendix D.

Table 3 lists the sources of the 3.6 μm data used in this analysis. Most of the images are from SINGS, the LVL Survey, or the Spitzer Survey of Stellar Structure in Galaxies (S^{4}G; Sheth et al. 2010). All data are in maps with pixel sizes of 1.5 arcsec. The FWHM of the PSF is 1.7 arcsec, and the calibration uncertainty is 3 per cent (IRAC Instrument and Instrument Support Teams 2013).[7] We multiplied the 3.6 μm data by the surface brightness correction factor 0.91 as recommended by the IRAC Instrument and Instrument Support Teams (2013). The 2MASS data are obtained from Jarrett et al. (2003). These data have pixel sizes of 1 arcsec, PSF FWHMs of 2–3 arcsec, and calibration uncertainties of 3 per cent.

3.4 Data preparation

The data preparation steps are almost identical to the steps applied by Bendo et al. (2012a). We began with identifying foreground stars in the Hα, 1.6 μm and 3.6 μm images, which appear as unresolved sources with very blue colours (with 3.6/24 μm flux density ratios $\gtrsim$10) or as sources with positive and negative counterparts in the Hα data. We then removed these sources by interpolating over them. We also removed residual continuum emission from the bulges in the Hα images of NGC 3031, 3953, 4548 and 4725, which we could identify as potential stellar emission because it was unusually diffuse compared to other sources within the galaxies or because we could see artefacts in the central regions (e.g. negative sources or asymmetric PSFs) that appeared similar to the artefacts associated with foreground stars. We also removed a couple of very bright stars that are visible in the 24 μm image on NGC 3621.

After this, we applied convolution kernels from Aniano et al. (2011) to match the PSFs of all of the data to the PSF of the 350 μm data, which has the largest FWHM. These kernels not only change the FWHM of the PSFs but also match the extended structure outside the central peak. Specific kernels were created for matching the IRAC 3.6 μm, *WISE* 22 μm, MIPS 24 μm, PACS 160 μm, and SPIRE 250 μm PSF to the SPIRE 350 μm PSF. For the other images, we assumed that the PSFs are approximately Gaussian and used kernels that match Gaussian functions to the SPIRE 350 μm PSF.

[6] http://wise2.ipac.caltech.edu/docs/release/allsky/expsup/

[7] http://irsa.ipac.caltech.edu/data/SPITZER/docs/irac/iracinstrumenthandbook/IRAC_Instrument_Handbook.pdf

Following this, we matched the coordinate systems of all images to the coordinates of the 350 μm data (which has 8 arcsec pixels). Next, we subtracted the background from the data using locations outside the optical discs of the galaxies. These data were used to produce 160/250 and 250/350 μm ratio maps that we used in the qualitative analyses in Section 4.

For quantitative analyses, we rebinned the data into 24 arcsec bins, which is both an integer multiple of the 250 or 350 μm map pixels and approximately equivalent to the FWHM of the data after convolution. The rebinning is performed in such a way that the centre of each galaxy will correspond to the centre of a bin. Since we are using data where the bins are equivalent to the FWHM of the PSF, these binned data will generally sample individual resolution elements in the data and will therefore be statistically independent.

NGC 3031 contains a low-luminosity active galactic nucleus that potentially produces non-thermal emission in these wavebands. We excluded the central 3 × 3 bins from the quantitative analyses, although we still show these data in the plots of the 24 arcsec binned data.

4 QUALITATIVE ANALYSIS OF FAR-INFRARED SURFACE BRIGHTNESS RATIOS

Fig. 1 shows the extinction-corrected Hα images (as a tracer of star formation), the 3.6 μm images (as a tracer of the evolved stellar population), and the 160/250 and 250/350 μm surface brightness ratios (shown as colour temperatures) for all galaxies in the sample. If dust is heated locally by star-forming regions, multiple unresolved hot regions will appear in the colour temperature maps in locations with strong star formation activity as seen in the Hα images, and the colour temperatures will also appear higher in structures with enhanced star formation activity such as spiral arms. If dust is heated locally by the evolved stellar population, then the colour temperatures will appear to decrease more smoothly with radius and will only appear locally enhanced in broader structures with enhanced 3.6 μm emission. This ignores the issue that the scaleheight of the stars, particularly the older stars, may be much larger than that of the dust, but given that the stellar emission drops exponentially (or more steeply) with height above the disc of the galaxy, the projected stellar emission should still approximate the radiation field of the stars intermixed with the dust.

The ratios are shown as colour temperatures as a useful reference for relating the ratios to SED shape. The actual temperatures of the dust seen at these wavelengths may differ depending on the dust emissivity and may have a broad range of temperatures, although the colour temperatures should be approximately similar to the mean temperature of dust emitting at any pair of wavelengths.

These maps demonstrate that the heating sources for dust vary significantly among nearby galaxies. The 160/250 μm colour temperature maps for about half the sample (NGC 628, 925, 2403, 3184, 3938, 4254, 4303, 4501, 4535, 4725, 5055, 5236, 5364, and 5457) appear more strongly associated with star-forming regions than with the structures traced by the evolved stellar population.

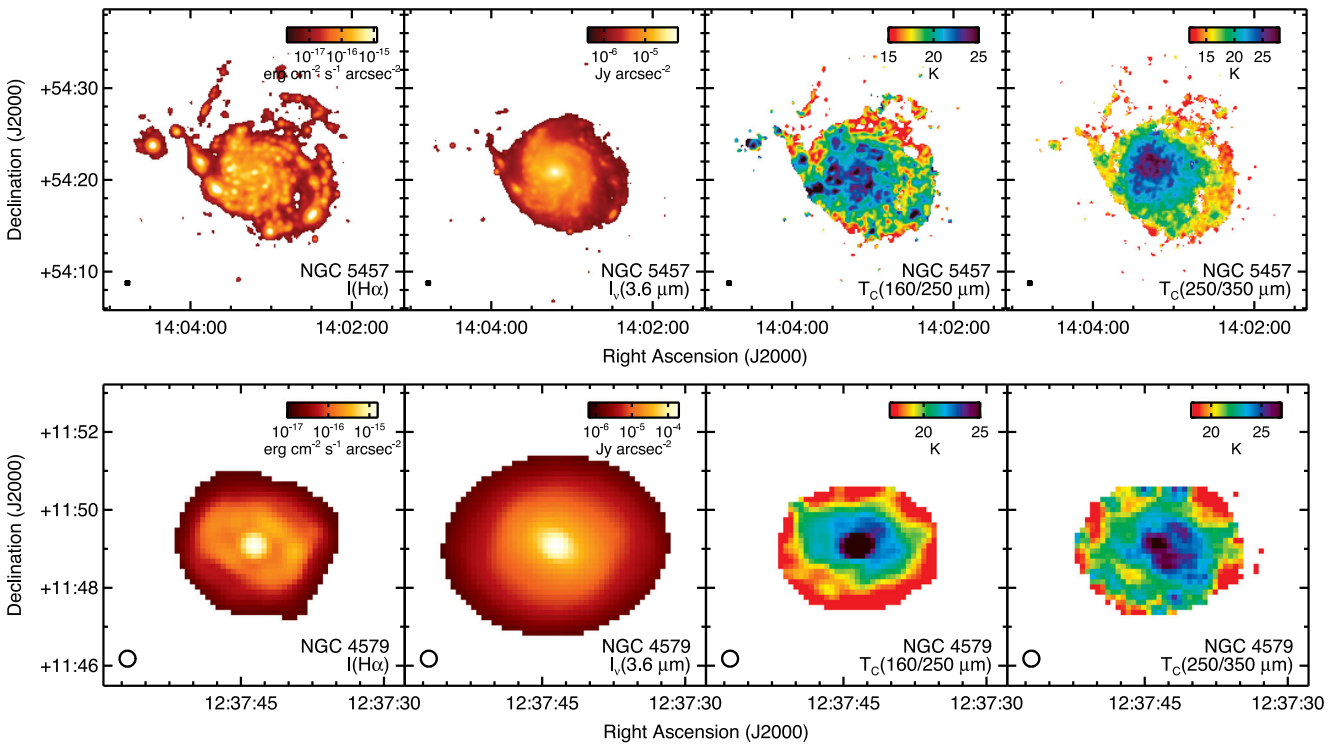

Figure 1. Hα, 3.6 μm, 160/250 μm, and 250/350 μm images of two example galaxies. NGC 5457 is an example of a galaxy where the smooth structures in the 250/350 μm ratio are more strongly related to those in the 3.6 μm image than in the Hα image, although the locally enhanced colour temperatures in the 160/250 μm map qualitatively appear more like the Hα image. NGC 4579 is an example of a galaxy where the 160/250 and 250/350 μm colour variations resemble structures in both the Hα and 3.6 μm images. Equivalent images for the other galaxies in the sample are available online. All images are based on data where the PSF has been matched to the PSF of the 350 μm image, which has an FWHM of 25 arcsec. The 160/250 and 250/350 μm ratios are shown as colour temperatures (based on modified blackbodies with λ^{-2} emissivities) so that the colours can be related to the SED shape, although the actual temperatures may vary. We only show data within approximately the optical disc of each galaxy detected at the 5σ level in the Hα or 3.6 μm maps or above the 3σ level in the colour temperature maps; other parts of the image are left blank. Images for the other galaxies in our sample are shown in the online version of this paper.

Additionally, the 250/350 μm colour temperatures for NGC 925, 4254, 4303, 4501, and 5364 also look more closely related to star-forming regions. In some cases, the colours clearly appear enhanced either in individual star-forming regions or in star-forming structures such as the spiral arms in NGC 5236. In NGC 4254 and 5055, the relation is also seen in the match between the asymmetric distribution of star formation and the asymmetric colour temperatures. In NGC 4254, 4303, and 4501, the relation of the colour temperature variations to star formation appears stronger than the relation to the evolved stellar population because the colour temperatures do not peak in the centre like the evolved stellar population does but instead appear enhanced in a broader region tracing the locations of enhanced star formation.

In contrast, the 250/350 μm colour temperatures in several galaxies (NGC 628, 2403, 3031, 3621, 3938, 3953, 5055, and 5457) trace structures that are similar to the emission seen at 3.6 μm. We can clearly see that the colour temperatures are not enhanced in star-forming regions that appear in the Hα maps in many of these galaxies. Instead, the colour temperatures tend to vary smoothly with radius. In the case of NGC 3031, 3621, and 3953, this applies to the 160/250 μm ratios as well. In NGC 628, 2403, 3938, 5055, and 5457, however, the 160/250 μm colours are strongly affected by star-forming regions; this result along with the result for the 250/350 μm ratios indicates that the transition from dust heated by star-forming regions to dust heated by evolved stars occurs between 160 and 250 μm for these galaxies.

In most of the rest of the galaxies, the interpretation of both of the colour temperature maps is ambiguous. The corrected Hα (or 24 μm) and 3.6 μm maps for NGC 3631, 4321, 4579, 4736, and 6946 trace structures that are not visually distinct enough to allow us to visually see differences between them or to see that the colour temperature maps are better related to one heating source instead of another. Meanwhile, the colour temperature maps of NGC 4548 and 7793 appear intermediate between the Hα and 3.6 μm maps.

Many of the colour temperature maps are affected by artefacts that make them more difficult to interpret. Artefacts from imperfectly matched PSFs appear around some very bright sources. Noise in the shorter wavelength data tends to create hotspots, especially near the edges of the regions detected at the 3σ level.

Sometimes the 250/350 μm colour temperatures appear enhanced in lopsided regions that do not correspond to enhancements in either the Hα or 3.6 μm surface brightness, most notably in NGC 4725, 5457, 6946, and 7793. It is unclear whether these structures are intrinsic to the galaxies or a result of either foreground cirrus structures or image processing artefacts. NGC 6946 is at a galactic latitude of ∼12 deg, so the enhanced 250/350 μm colour temperatures on the east side of the galaxy could be the result of foreground cirrus structure. To investigate this further, we examined the dust optical depths at 353 GHz ($\tau_{353\,\mathrm{GHz}}$) from version R1.20 of the *Planck* thermal dust model map[8] (Planck Collaboration XIX 2011). For NGC 6946, the mean and standard deviation in the background values of $\tau_{353\,\mathrm{GHz}}$ (measured in an annulus 1.5–2.0 times the optical diameter of the galaxy specified in Table 1) were $(1.9 \pm 0.2) \times 10^{-5}$. For the other sample galaxies, the mean background values of $\tau_{353\,\mathrm{GHz}}$ were 0.6–5.1 $\times 10^{-6}$, a factor of ∼10 lower than for NGC 6946, and the standard deviations in $\tau_{353\,\mathrm{GHz}}$ for the other sample galaxies (0.2–1.3 $\times 10^{-6}$) were also lower than the standard deviation for NGC 6946. These results imply that foreground cirrus structures could be responsible for the structures in the NGC 6946 250/350 μm colour temperature maps. NGC 4725, 5457, and 7793, however, are at higher latitudes where cirrus structures should not have as much of an effect on the data. Moreover, the mean and standard deviation in the background $\tau_{353\,\mathrm{GHz}}$ values for these galaxies are actually below the median values for the sample overall, so it is unlikely that lopsided structures in the colour temperature maps of these galaxies are related to foreground cirrus emission.

The origin of the elongated structure in the 250/350 μm colour temperature map of NGC 5236 is unclear. It could be caused by actual enhancements in the colour temperatures, an artefact in one of the scans (some of which are aligned with the galaxy's bar), or a combination of these effects.

In the 160/250 μm colour temperature map for a few galaxies, particularly NGC 5236 and 6946, we can see small offsets between the spiral arm structures traced by the star-forming regions and the structures traced by the 160/250 μm ratios. This could potentially be the result of either the non-axisymmetric propagation of light from star-forming regions within the spiral arms in these galaxies or dust heating by a population of B and A stars that have migrated out of the star-forming regions in the spiral arms. This is discussed further in Appendix E.

5 ONE-ON-ONE COMPARISON OF FAR-INFRARED SURFACE BRIGHTNESS RATIOS TO HEATING SOURCES

We use the binned data to examine the quantitative relationship between the 160/250 and 250/350 μm ratios and potential dust heating sources. This analysis relies upon three assumptions. First, we assume that projection effects do not significantly affect the results; the remarkable correlation between the infrared surface brightness ratios and the stellar surface brightness found previously by Bendo et al. (2012a) in M81, which has a relatively large bulge, would suggest that this is not a significant issue. Secondly, we assume that the dust observed within the 24 arcsec bins is heated by the stars observed within those bins. As discussed in Appendix E, the physical sizes of the bins are usually larger than the mean free path of light. In the closest galaxies in the sample, the bins may be smaller than the mean free path of light, and if the light propagates asymmetrically from star-forming regions, as may be the case in some nearby grand-design spiral galaxies (see Appendix E), this assumption may not work well. Thirdly, we assume that the dust properties themselves are not variable. Some authors have also suggested that β is variable and also affects the far-infrared colours, although these variations may be related to a degeneracy with temperature in SED fitting (Shetty et al. 2009; Galametz et al. 2012; Kirkpatrick et al. 2014).

When comparing a ratio to a heating source, we only selected data that are detected at the 3σ level in the ratio that we wish to compare, the 3.6 μm band, and the star formation tracer (either the extinction-corrected Hα emission calculated using equation (1) or, when Hα data were not available, the 24 μm band).[9] As an additional step to

[8] Available from http://irsa.ipac.caltech.edu/data/Planck/release_1/all-sky-maps/previews/HFI_CompMap_ThermalDustModel_2048_R1.20/index.html.

[9] For clarity, when both Hα and 24 μm data were available for a galaxy, we did not require that both the uncorrected Hα and 24 μm emission were detected at the 3σ level when selecting data for the analysis in Section 5. We only required that the extinction-corrected Hα emission calculated using equation (1) was measured at the 3σ level. Hence, our analysis includes data from both strongly obscured and unobscured star-forming regions.

filter out low signal-to-noise data, we only use data from locations where the ratio is measured at the 3σ level both before and after rebinning the data into 24 arcsec bins. We often have more data points in the comparisons including the 250/350 μm ratios because those data have higher signal-to-noise levels in general.

For the analysis in this section, we use extinction-corrected Hα emission as a star formation tracer when it is available or the 24 μm emission otherwise. In Appendix A, we show how the results change when using either the uncorrected Hα or 24 μm surface brightnesses as alternative star formation tracers. In galaxies where we do not identify significant central 24 μm emission without corresponding Hα emission, the selection of star formation tracers only has a marginal effect on the results except for NGC 628, 3184, 3938, 5364, and 7793. We will mention these exceptions in the discussion and otherwise rely upon the results with the corrected Hα intensities.

Because we are working with galaxies at different distances, we also include an analysis in Appendix F that demonstrates how the results change for NGC 3031 and 5457 (the two galaxies in the sample with the largest angular sizes) when data are measured in bins that are 120 arcsec in size. Using these data, we would reach the same conclusions regarding the dust heating sources for these two galaxies as we would using the 24 arcsec bins, demonstrating that the analysis is relatively robust against resolution effects.

The relations between the infrared surface brightness ratios and either 3.6 μm emission or the best available star formation tracer are shown in Figs 2–5. For modified blackbody emission from dust with a temperature range similar to what is seen in the far-infrared in these galaxies, the relation between far-infrared surface brightness ratios and energy absorbed and re-emitted can be approximated by a power law to within a few per cent. Hence, we frequently see linear relations between the surface brightness ratios and the dust heating sources plotted in these figures. However, more scatter is seen at the low surface brightness end of the plots. To assess the strength of these relations (by examining which relations for each surface brightness ratio show less scatter), we do not necessarily need to use a non-parametric correlation coefficient (e.g. the Spearman correlation coefficient) because the relations in logarithm space are typically linear, but we do need to compensate for the variation in the signal-to-noise of the data in the relations. We therefore used the weighted Pearson correlation coefficients (Pozzi, Di Matteo & Aste 2012), where the uncertainties in the logarithm of the surface brightness ratios are used to weight the data (as the uncertainties in the 3.6 μm emission or star formation tracer in comparison to the dynamical range of the data are generally less significant). The weighted correlation coefficients for the relations in Figs 2–5 are given in Table 4. We interpret differences of 0.05 in the correlation coefficients as indicating that one heating source was more strongly linked to dust heating than the other. This is greater than the variation in the coefficients we have seen when using different versions of the *Herschel* data, when making adjustments to the data selection criteria, or when making adjustments to the astrometry.

Based on these criteria, we can clearly identify the 160/250 μm ratios as being better correlated with star formation tracers than with 3.6 μm emission in 8 out of 24 galaxies. Additionally, we see that the 250/350 μm ratios are also better correlated with star formation tracers in NGC 4303, 4501, and 5364 which would indicate that dust heated by star formation is the dominant source of emission at 250 μm and possibly even at longer wavelengths, although the results for NGC 4303 and 5364 depend on the star formation tracer used as discussed in Appendix A. NGC 628, 2403, and 5457 are the cases where the 160/250 μm ratios are clearly better correlated with star formation while the 250/350 μm ratios are clearly more strongly correlated with the evolved stellar population, which demonstrates a clear switch in dust heating sources between 160 and 250 μm. In the other galaxies, we can clearly identify star-forming regions as having the stronger influence on the 160/250 μm ratios, but the identification of which source more strongly affects the 250/350 μm ratios is more ambiguous or dependent on the star formation tracer used.

In 9 of the 24 galaxies within the sample, the 250/350 μm ratios are more strongly correlated with the 3.6 μm emission than with star formation, indicating that in about half of the galaxies, the dust seen at $\geq$250 μm is heated by the evolved stellar population. NGC 3621 and 4548 are odd cases where the two correlation coefficients in Table 4 for the 250/350 μm ratio differ only by $<$0.05 but where the data for the 160/250 μm ratio show that the ratio is more strongly correlated with 3.6 μm emission, implying that the emission at $\leq$160 μm is from dust heated by the evolved stellar population. (We at least do not see any case where the 250/350 μm ratios are clearly related to star formation while the 160/250 μm ratio is more strongly related to the 3.6 μm band tracing the evolved stellar population.) Aside from NGC 3621 and 4548, we also find that the 160/250 μm ratios for NGC 3031, 4725, and 7793 are also well correlated with the 3.6 μm emission. In the other galaxies, we find either that the 160/250 μm ratios are more clearly correlated with star formation tracers or that we cannot clearly relate the 160/250 μm ratios to a heating source.

In eight galaxies, we see no clear difference in the way both the 160/250 and 250/350 μm ratios are related to either dust heating source based on this analysis alone. In many of these galaxies, this is because the extinction-corrected Hα emission is very well correlated with the 3.6 μm emission as measured within the 24 arcsec binned data. The rightmost column in Table 4 shows that the correlation coefficients for the relation between the logarithms of the Hα and 3.6 μm emission for seven of these eight galaxies are $>$0.90; the lowest value is 0.84 for NGC 3938. Hence, surface brightness ratios measured in the 24 arcsec binned data for these galaxies will tend to look equally correlated with both tracers of different dust heating sources in these galaxies. In contrast, the correlation coefficients for the relations between Hα and 3.6 μm emission are $\leq$0.90 for all galaxies where we can definitely identify a stronger relation between one of the dust heating sources and the surface brightness ratios.

In the eight galaxies where we have difficulty statistically identifying a dominant dust heating source, the qualitative analysis on the colour temperature maps in Section 4 implies that the 160/250 μm ratios for NGC 3938, 4535, 5055, and 5236 are more closely related to star formation while the 250/350 μm ratios for NGC 3938 and 5055 are more closely related to the evolved stellar population. However, given the issues encountered in the analysis here, it may be that these qualitative interpretations are overly subjective. The qualitative results based on the 250/350 μm maps for NGC 4535 and 5236 as well as the results for both ratio maps for NGC 3631, 4321, 4579, and 6946 are as ambiguous as the results from the statistical approach.

The quantitative approach used in this section generally implies that the contribution of the evolved stellar populations to dust heating is higher than what is indicated by the qualitative analysis of the colour temperature maps in Section 4. We may have obtained this result for a few reasons. First, we may be visually sensitive to picking out compact locations with hotter colours in the maps, which would tend to bias us towards identifying the surface brightness variations as being more strongly related qualitatively to star

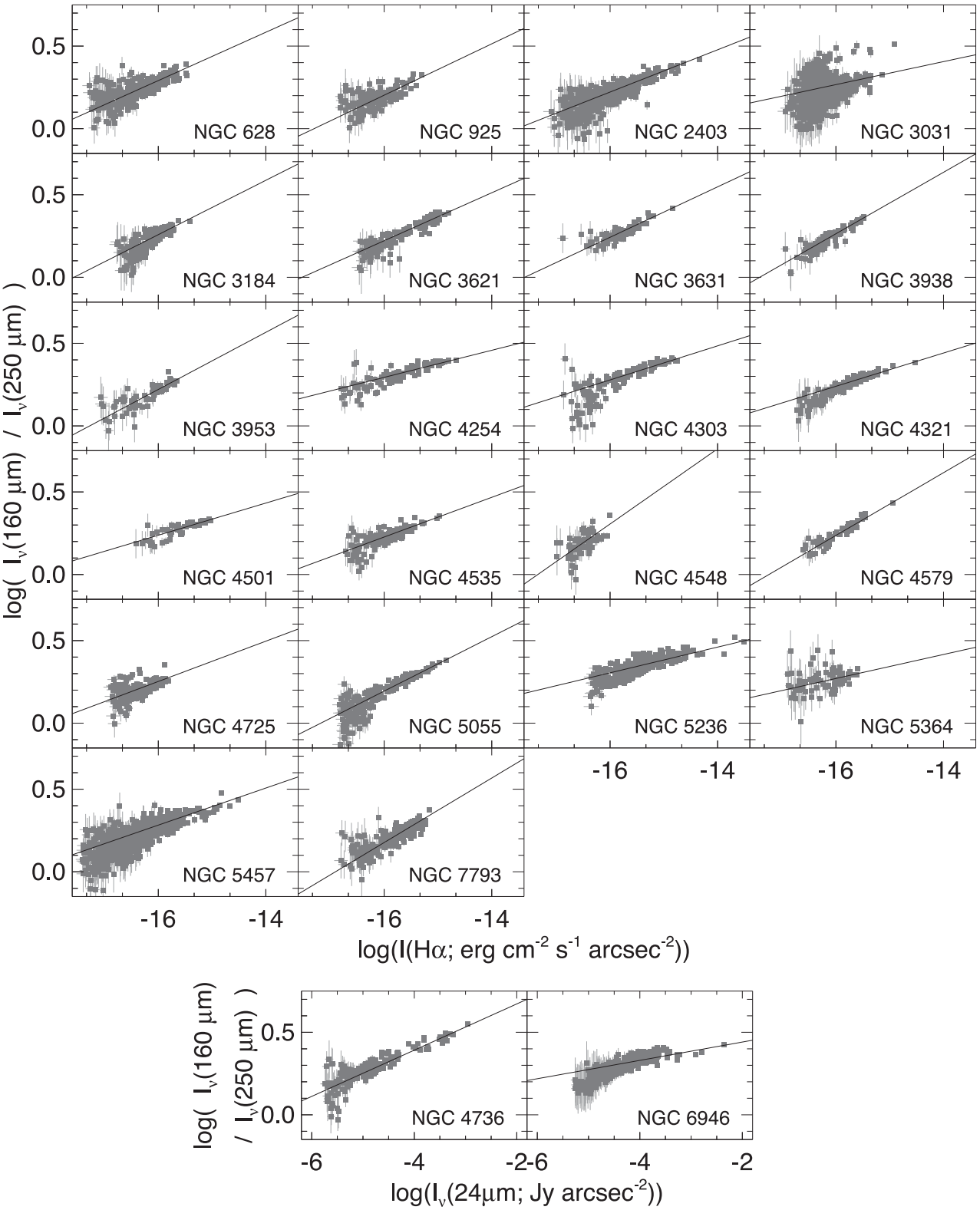

Figure 2. Plots of 160/250 μm surface brightness ratios versus extinction-corrected Hα intensities (top) and, for galaxies with no available Hα data, 24 μm surface brightnesses (bottom) measured in the 24 arcsec binned data. Only data detected at above the 3σ level in the plotted ratio, the 3.6 μm emission, and the star formation tracer (either the extinction-corrected Hα emission or, when Hα data were not available, the 24 μm emission) are shown; see the text of Section 5 for additional details. The solid lines show the best-fitting lines. Table 4 gives the weighted Pearson correlation coefficients for the relations in these plots.

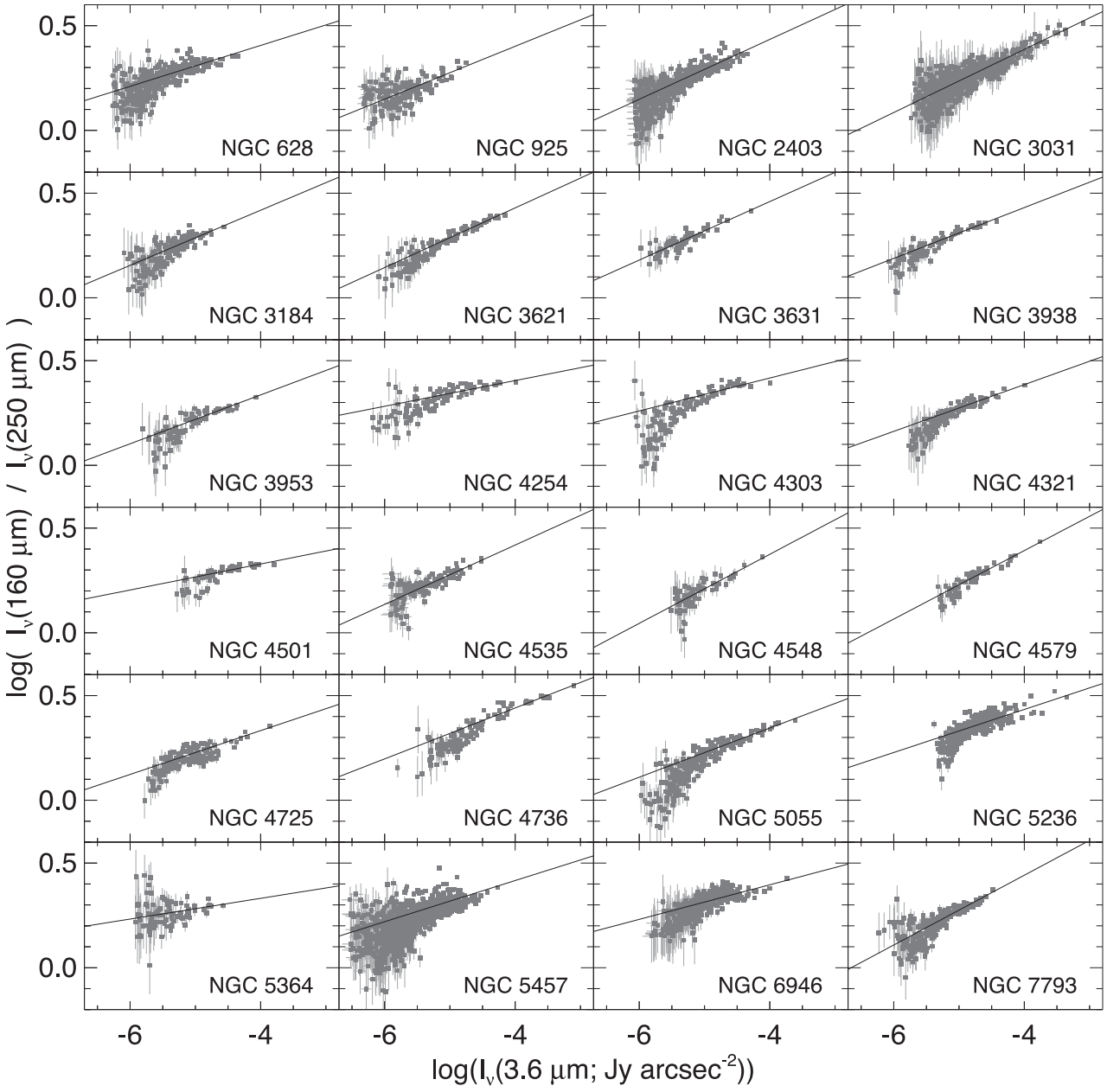

Figure 3. Plots of 160/250 μm surface brightness ratios versus 3.6 μm surface brightnesses measured in the 24 arcsec binned data. See the caption for Fig. 2 for additional details regarding this figure.

formation. Secondly, the evolved stellar populations will have a smoother distribution than the star-forming regions and will tend to decrease smoothly with radius. This type of gradient can be difficult to pick out visually, but correlations between radially varying quantities are easy to detect statistically.

6 DECOMPOSITION OF FAR-INFRARED SURFACE BRIGHTNESS RATIO VARIATIONS INTO SEPARATE COMPONENTS

As an alternative approach for identifying the heating source for the dust, we fit the 160/250 and 250/350 μm surface brightness ratios to a combination of the 3.6 μm emission and one of the star formation tracers using

$$\ln\left(\frac{I_\nu(\lambda_1)}{I_\nu(\lambda_2)}\right) = \alpha \ln(I(\mathrm{SFR}) + A_1 I_\nu(3.6\,\mu\mathrm{m})) + A_2 \quad (2)$$

derived by Bendo et al. (2012a) from the Stefan–Boltzmann law upon the assumptions that the dust temperatures in the pairs of bands used here can be approximated as a single temperature and that the relation between dust temperature and either far-infrared ratio can be approximated by a power law. $I_\nu(\lambda_1)/I_\nu(\lambda_2)$ is the far-infrared surface brightness ratio. I(SFR) is the emission from the star formation tracer, which is related to the energy E_{SF} from the star-forming regions, and $I_\nu(3.6\,\mu\mathrm{m})$ is the surface brightness at 3.6 μm, which is related to the energy E_{ES} from the evolved stellar

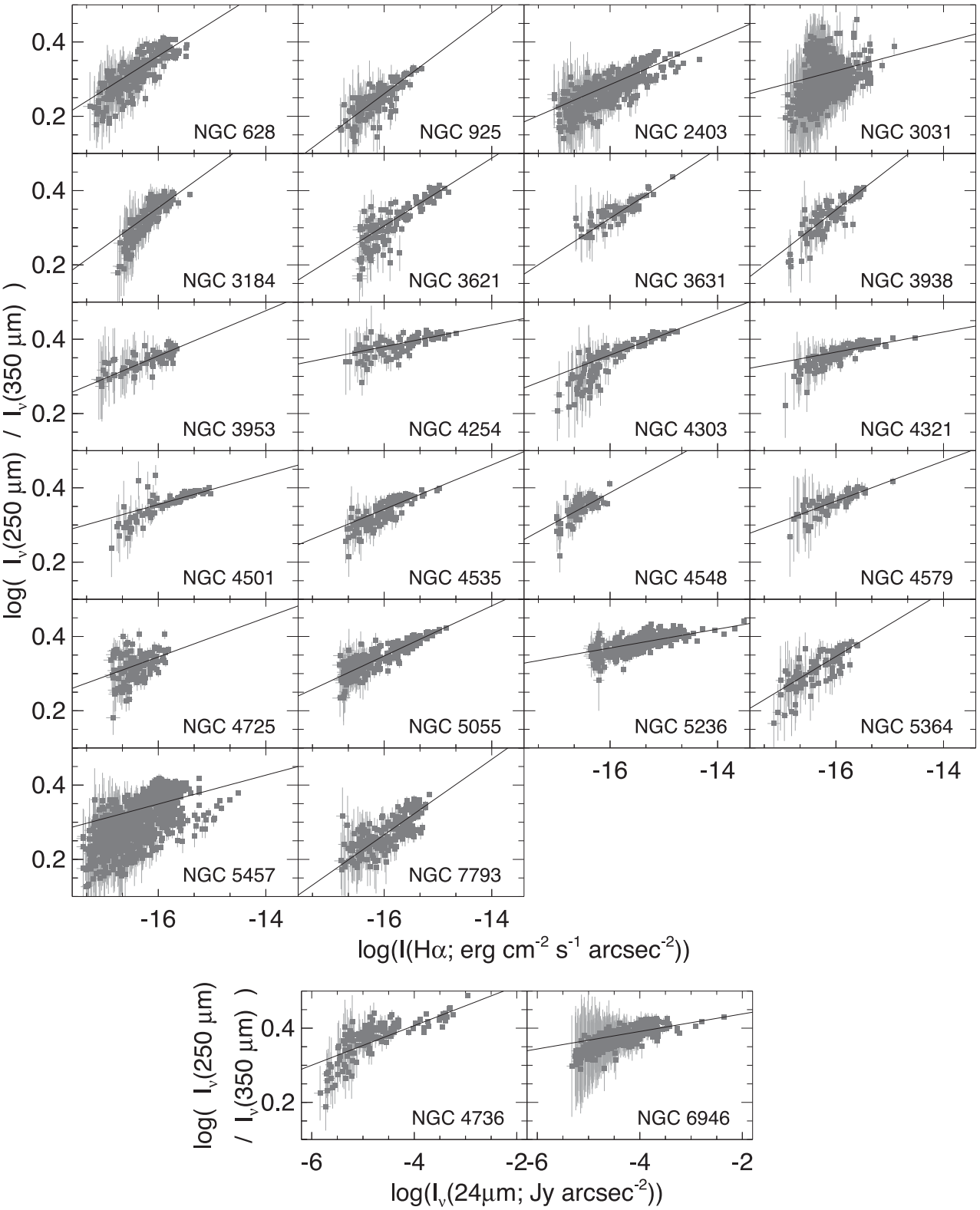

Figure 4. Plots of 250/350 μm surface brightness ratios versus extinction-corrected Hα intensities (top) and, for galaxies with no available Hα data, 24 μm surface brightnesses (bottom) measured in the 24 arcsec binned data. See the caption for Fig. 2 for additional details regarding this figure.

population. The terms α, A_1, and A_2 are derived in the fit. In fitting this equation to the far-infrared ratios, we effectively decompose the ratios into star formation and evolved stellar population components. As a result, we can calculate the contribution of evolved stellar population to the total dust heating $E_{\rm Tot}$ using

$$\eta(\lambda_1/\lambda_2) = \frac{E_{\rm ES}}{E_{\rm Tot}} = \frac{A_1 I_\nu(3.6\,\mu{\rm m})}{I({\rm H}\alpha) + A_1 I_\nu(3.6\,\mu{\rm m})}. \quad (3)$$

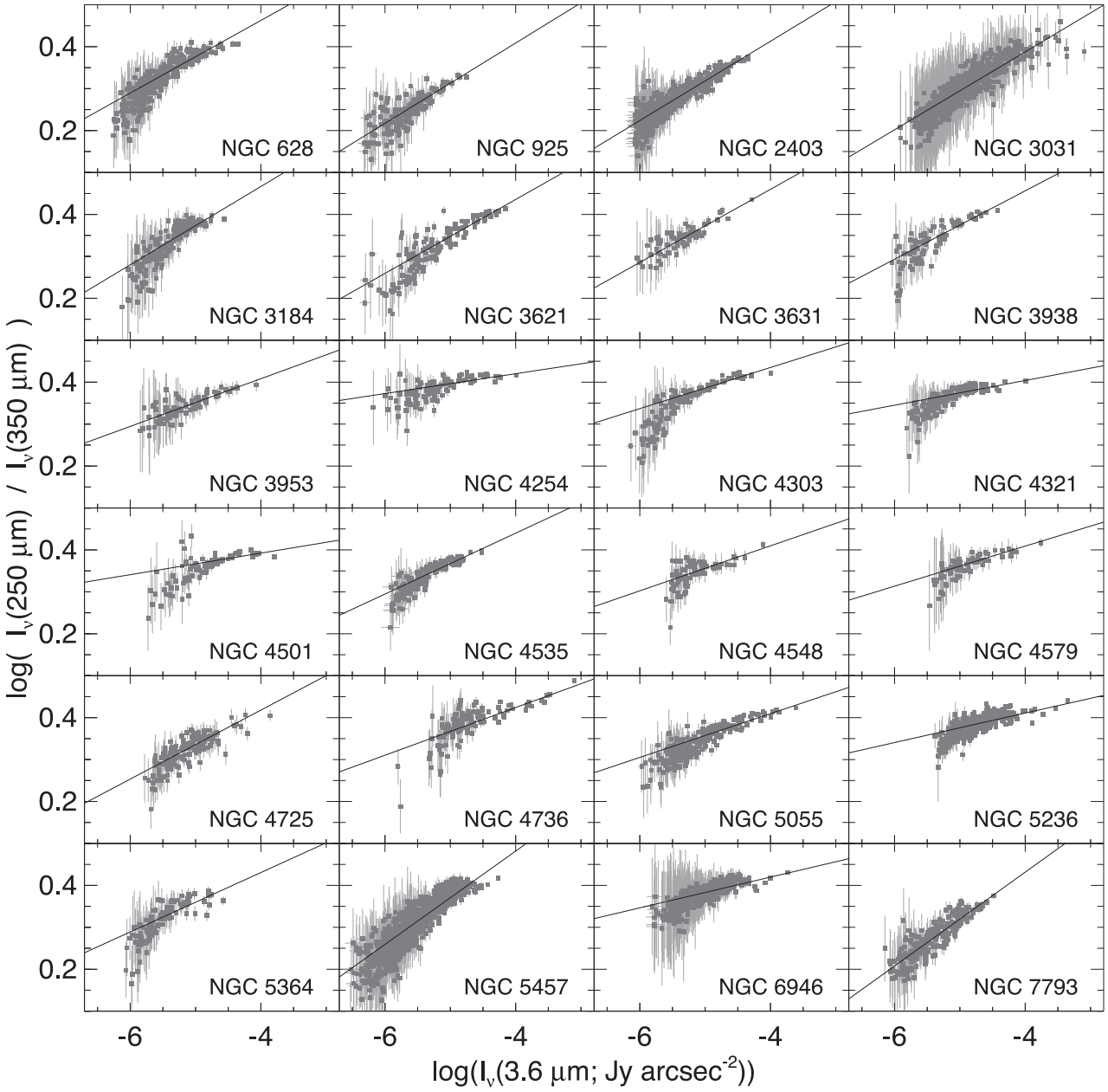

Figure 5. Plots of 250/350 μm surface brightness ratios versus 3.6 μm surface brightnesses measured in the 24 arcsec binned data. See the caption for Fig. 2 for additional details regarding this figure.

In practice, $\eta(\lambda_1/\lambda_2)$ also indicates that the relative fraction of the emission in the λ_1 band originates from dust heated by the evolved stellar population, at least as long as λ_2 is located on the Rayleigh–Jeans side of the dust SED. This is because $I_\nu(\lambda_1)/I_\nu(\lambda_2)$ is equivalent to $I_\nu(\lambda_1)$ normalized for dust mass, in which case it only depends on dust temperature. In Appendix G, we perform some tests with simplified models of dust heating in galaxies in which we test the effectiveness of using $\eta(\lambda_1/\lambda_2)$ to rescale the 160 and 250 μm emission. We generally find that the numbers are accurate to within 0.15, although the derived η may decrease with distance, as discussed below.

Table 5 shows the best-fitting parameters to equation (2) for each galaxy for each surface brightness ratio as well as the resulting η values. The values and uncertainties are derived using a Monte Carlo approach. We perform a least-squares fit to equation (2) in 10 000 iterations in which Gaussian noise (scaled based on the measured standard deviations in the binned data) has been added to both the ratios and the tracers of dust heating sources, and then we determine the median and standard deviation for each of the parameters and η after removing 5σ outliers. For fitting each ratio, we selected 24 arcsec bins within the optical disc of each galaxy where either the 3.6 μm or star formation tracer was detected at the 3σ level and where the far-infrared ratio was measured at the 3σ level. The extinction-corrected Hα data are used to trace heating by star-forming regions except for NGC 4736 and 6946, where we used 24 μm data because suitable Hα data were not available. The uncertainties for A_1 may sometimes be very large, but η is frequently better constrained because it is also dependent upon the magnitude of $A_1 I_\nu(3.6\ \mu\mathrm{m})$ relative to I(SFR). We did find a strong degeneracy between A_2 and α as well as much weaker degeneracies between A_1

Table 4. Weighted correlation coefficients for relations between 160/250 and 250/350 μm ratios and tracers of heating sources.

Galaxy	Weighted correlation coefficients				
	$\log(I_\nu(160\,\mu m)/I_\nu(250\,\mu m))$		$\log(I_\nu(250\,\mu m)/I_\nu(350\,\mu m))$		$\log(I_\nu(3.6\,\mu m))$
	versus $\log(I(H\alpha))^a$	versus $\log(I_\nu(3.6\,\mu m))$	versus $\log(I(H\alpha))^a$	versus $\log(I_\nu(3.6\,\mu m))$	versus $\log(I(H\alpha))^a$
NGC 628	0.82	0.71	0.75	0.87	0.53
NGC 925	0.82	0.77	0.88	0.88	0.73
NGC 2403	0.92	0.81	0.75	0.94	0.48
NGC 3031	0.17	0.84	0.16	0.87	0.14
NGC 3184	0.81	0.79	0.76	0.81	0.85
NGC 3621	0.88	0.96	0.89	0.90	0.80
NGC 3631	0.95	0.96	0.95	0.96	0.99
NGC 3938	0.96	0.93	0.88	0.89	0.84
NGC 3953	0.83	0.84	0.71	0.86	0.63
NGC 4254	0.88	0.81	0.69	0.68	0.96
NGC 4303	0.88	0.73	0.90	0.84	0.78
NGC 4321	0.97	0.96	0.85	0.82	0.99
NGC 4501	0.86	0.75	0.82	0.64	0.90
NGC 4535	0.91	0.89	0.87	0.91	0.92
NGC 4548	0.67	0.91	0.69	0.73	0.70
NGC 4579	0.96	0.95	0.84	0.81	0.97
NGC 4725	0.48	0.75	0.38	0.77	0.35
NGC 4736	0.95^b	0.94	0.81^b	0.91	0.92^b
NGC 5055	0.98	0.95	0.94	0.92	0.96
NGC 5236	0.89	0.87	0.82	0.83	0.98
NGC 5364	0.43	0.37	0.79	0.74	0.75
NGC 5457	0.89	0.57	0.40	0.89	0.40
NGC 6946	0.89^b	0.86	0.81^b	0.83	0.99^b
NGC 7793	0.85	0.90	0.72	0.87	0.68

Note: [a]The Hα data used here were corrected for extinction using 24 μm data.
[b]No Hα data were available for these galaxies. These coefficients are based on relations between the infrared surface brightness ratios and 24 μm emission.

and the other parameters. This is illustrated by Fig. 6, which shows the range of the best-fitting parameters for the 160/250 μm data for NGC 628. However, these plots also show that the fitting procedure will converge upon a single best-fitting value rather than converging upon a local minimum in χ^2.

We had a few galaxies where the fits produced results where one of the heating source terms in equation (2) [either I(SFR) or $A_1 I_\nu(1.6\,\mu m)$] was negligible compared to the other term. In these situations, we performed a linear fit between $\ln(I_\nu(\lambda_1)/I_\nu(\lambda_2))$ and the logarithm of the heating source. In most cases, we used the heating source which was better correlated with the surface brightness ratio according to the results in Table 4. For the 250/350 μm ratio for NGC 4254 and the 160/250 μm ratio for NGC 6946, however, the correlation coefficients in Table 4 do not clearly demonstrate that one heating source is dominant. In these cases, the rms residuals from fits between the ratios and the star formation tracer are smaller than those for the corresponding fits with the 3.6 μm emission, so we quote results in Table 5 based on the fit to the star formation tracer, although these particular results should be treated somewhat cautiously.

In addition to the tabular data, Fig. 7 shows the observed surface brightness ratio maps for each galaxy, the surface brightness ratios from best-fitting parameters in Table 5, the residuals from the fit (shown as the difference between the observed and fitted colour temperature maps), and maps of η based on the fits. The levels in the residual images are scaled roughly by the total dynamic range in the colour temperatures of the observed data and can be used to assess the quality of the fits. Residual images for good fits will either look like noise or reveal imaging artefacts.

The results show a broad spread in the relative contributions of star-forming regions and the evolved stellar population to dust heating. We found 10 galaxies where $\eta(160/250\,\mu m) < 0.30$, and 6 of these galaxies have $\eta(250/350\,\mu m) < 0.30$. In contrast, we found 11 galaxies (excluding NGC 6946 for reasons discussed below) with either $\eta(160/250\,\mu m) > 0.70$ or $\eta(250/350\,\mu m) > 0.70$, which would indicate that the evolved stellar population is the dominant heating source for dust seen at least at ≥250 μm. For five galaxies, we find that $0.30 < \eta < 0.70$ for both the 160/250 and 250/350 μm ratios, which would indicate that star-forming regions and the evolved stellar populations equally contribute to heating the dust seen at 160–350 μm. However, just because this ratio is near 0.50 for an individual galaxy does not necessarily mean that star-forming regions and the evolved stellar population contribute equally to dust heating everywhere within that galaxy. Several of the η maps, such as the 160/250 μm maps for NGC 925, 2403, and 5457, show that star-forming regions may be dominant local dust heating sources but that dust seen in diffuse regions or near the centres of the galaxies at these wavelengths is heated more by light from the evolved stellar population. We also see in the 160/250 μm maps for NGC 4725 and 4736 that star-forming regions may contribute more to heating dust within ring-like structures seen at these wavelengths but that the evolved stellar population contributes more to the dust heating in other locations.

For the majority of galaxies in this analysis, $\eta(160/250\,\mu m)$ is smaller than $\eta(250/350\,\mu m)$. This matches our expectations, as we would expect to see dust heated by star-forming regions at shorter wavelengths and dust heated by evolved stars at longer wavelengths. The result also gives us more confidence in the results from using this multiple component fit to identify heating sources. In NGC 3621, 4321, and 4548, however, $\eta(250/350\,\mu m)$ was significantly smaller ($\gtrsim$0.15) than $\eta(160/250\,\mu m)$. The 250/350 μm residual images from the fits applied to both NGC 3621 and 4548 show

Table 5. Results from fitting equation (2) to the 160/250 and 250/350 μm surface brightness ratios.

Galaxy	Results for fits to I_ν(160 μm)/I_ν(250 μm)				Results for fits to I_ν(250 μm)/I_ν(350 μm)			
	A_1[a]	A_2	α	η	A_1[a]	A_2	α	η
NGC 628	4.7 ± 0.6	5.8 ± 0.1	0.141 ± 0.003	0.25 ± 0.02	53.7 ± 17.0	4.0 ± 0.1	0.089 ± 0.003	0.77 ± 0.05
NGC 925	22.0 ± 4.8	6.0 ± 0.2	0.152 ± 0.006	0.40 ± 0.05	41.6 ± 15.8	4.4 ± 0.2	0.106 ± 0.006	0.54 ± 0.08
NGC 2403	29.0 ± 2.5	5.8 ± 0.1	0.147 ± 0.002	0.48 ± 0.02	634.9 ± 225.4	3.7 ± 0.1	0.090 ± 0.002	0.94 ± 0.02
NGC 3031	31.0 ± 4.6	6.5 ± 0.2	0.167 ± 0.005	0.79 ± 0.02	186.9 ± 134.7	4.2 ± 0.2	0.103 ± 0.006	0.95 ± 0.03
NGC 3184	11.5 ± 3.2	6.1 ± 0.3	0.153 ± 0.007	0.41 ± 0.06	31.7 ± 19.0	4.2 ± 0.3	0.094 ± 0.007	0.65 ± 0.12
NGC 3621	77.2 ± 9.9	5.9 ± 0.1	0.151 ± 0.002	0.73 ± 0.02	36.2 ± 6.8	4.1 ± 0.1	0.093 ± 0.002	0.56 ± 0.04
NGC 3631	67.4 ± 20.0	5.7 ± 0.1	0.143 ± 0.004	0.67 ± 0.08	40.1 ± 25.6	3.9 ± 0.2	0.088 ± 0.005	0.55 ± 0.17
NGC 3938	6.1 ± 2.2	6.6 ± 0.3	0.165 ± 0.007	0.25 ± 0.06	16.1 ± 14.2	4.2 ± 0.3	0.094 ± 0.008	0.46 ± 0.17
NGC 3953	5.1 ± 1.7	6.2 ± 0.5	0.157 ± 0.013	0.38 ± 0.07	23.4 ± 23.2	2.8 ± 0.3	0.056 ± 0.009	0.72 ± 0.17
NGC 4254	0.0[b]	4.5 ± 0.3	0.103 ± 0.008	0.00	0.0[b]	2.3 ± 0.3	0.040 ± 0.008	0.00
NGC 4303	0.0[b]	6.1 ± 0.3	0.149 ± 0.008	0.00	7.4 ± 4.3	2.8 ± 0.1	0.054 ± 0.002	0.21 ± 0.09
NGC 4321	5.3 ± 3.3	4.3 ± 0.1	0.102 ± 0.002	0.20 ± 0.09	0.0[b]	3.0 ± 0.3	0.059 ± 0.008	0.00
NGC 4501	0.0[b]	4.7 ± 0.7	0.115 ± 0.018	0.00	0.0[b]	3.2 ± 0.3	0.064 ± 0.009	0.00
NGC 4535	16.6 ± 5.0	5.2 ± 0.1	0.129 ± 0.004	0.40 ± 0.07	66.2 ± 19.5	3.2 ± 0.1	0.068 ± 0.004	0.72 ± 0.07
NGC 4548	20.6 ± 16.6	6.6 ± 0.6	0.170 ± 0.016	0.82 ± 0.09	3.1 ± 1.9	3.4 ± 0.4	0.069 ± 0.009	0.43 ± 0.12
NGC 4579	5.5 ± 1.7	7.2 ± 0.2	0.183 ± 0.006	0.42 ± 0.07	5.4 ± 6.1	2.6 ± 0.3	0.049 ± 0.008	0.42 ± 0.20
NGC 4725	5.0 ± 0.5	6.5 ± 0.2	0.164 ± 0.006	0.46 ± 0.02	12.8 ± 3.8	4.3 ± 0.2	0.098 ± 0.006	0.66 ± 0.06
NGC 4736[c]	1.8 ± 0.1	2.1 ± 0.1	0.137 ± 0.001	0.50 ± 0.02	[d]	1.8 ± 0.1	0.084 ± 0.007	1.00
NGC 5055	0.0[b]	7.3 ± 0.2	0.188 ± 0.006	0.00	3.3 ± 1.5	3.1 ± 0.1	0.063 ± 0.002	0.24 ± 0.08
NGC 5236	4.1 ± 0.5	3.6 ± 0.0	0.080 ± 0.000	0.14 ± 0.01	373.5 ± 202.5	2.0 ± 0.0	0.034 ± 0.001	0.92 ± 0.04
NGC 5364	5.4 ± 6.1	2.5 ± 0.6	0.051 ± 0.016	0.26 ± 0.16	4.0 ± 4.3	3.7 ± 0.3	0.079 ± 0.008	0.21 ± 0.14
NGC 5457	10.0 ± 0.5	5.3 ± 0.1	0.129 ± 0.001	0.37 ± 0.01	[d]	2.5 ± 0.1	0.139 ± 0.004	1.00
NGC 6946[c]	0.0[b]	1.9 ± 0.1	0.123 ± 0.008	0.00	73 ± 96	1.3 ± 0.0	0.054 ± 0.005	0.92 ± 0.07[e]
NGC 7793	50.7 ± 7.1	7.3 ± 0.2	0.192 ± 0.005	0.60 ± 0.03	401.2 ± 210.0	4.4 ± 0.2	0.111 ± 0.004	0.92 ± 0.04

Note: [a]A_1 has units of 10^{-12} erg cm^{-2} s^{-1} Jy^{-1} unless otherwise noted.
[b]For these fits, $A_1 I_\nu$(3.6 μm) in equation (2) was found to be negligible compared to I(SFR). We therefore report A_1 as 0. The A_2 and α values are based on fitting the star formation tracer to the infrared surface brightness ratio using a power law.
[c]Hα data were not for these galaxies, so we used 24 μm data as a substitute star formation tracer. A_1 in these cases is dimensionless.
[d]For these fits, I(SFR) in equation (2) was found to be negligible compared to $A_1 I_\nu$(3.6 μm). We therefore fit ln(I_ν(250 μm)/I_ν(350 μm)) to ln(I_ν(3.6 μm)) using a linear function. The α listed here is the slope, and A_2 is the constant.
[e]The η(250/350 μm) values for this galaxy are suspect. See the text in Section 6 for details.

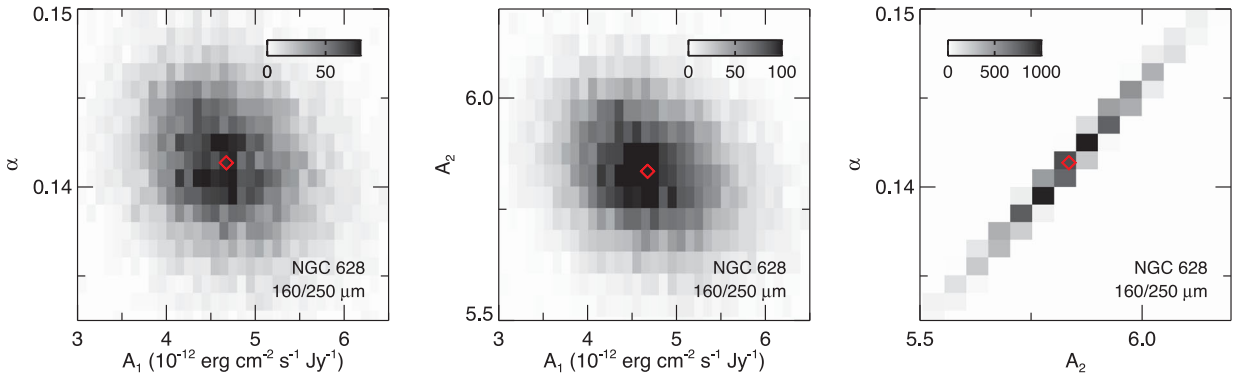

Figure 6. Plots showing the distributions of best-fitting parameters when using a Monte Carlo approach to fit equation (2) to the 160/250 μm data for NGC 628. For illustration purposes, the parameter space has been divided into multiple bins, and the shades of grey indicate the number of iterations that produce parameters that fall within each of these bins. The results are based on 10 000 iterations. The red diamond shows the median parameters.

some broad asymmetric structures that were not fitted using equation (2) properly and could potentially have caused issues with the fits in these two specific cases. The reason for the inconsistencies in NGC 4321 are probably the result of the I_ν(3.6 μm) term being relatively small compared to the I(SFR) term for the 250/350 μm ratio.

The 250/350 μm data of NGC 6946 stand out as a special case where we had difficulty accurately reproducing the observed colour temperature structures. Neither the star-forming regions (traced by the 24 μm data in this case) nor the evolved stellar populations trace the structures seen in the 250/350 μm map, so we would naturally not be able to fit this as the function of the sum of the 3.6 and 24 μm data. We therefore flag the η(250/350 μm) value as suspect in Table 5 and disregard it in the rest of the analysis.

As a consistency check, we can compare the η values for NGC 2403, 3031, and 5236 to the η values from Bendo et al. (2012a). They expressed their results as E_{SF}/E_{Tot}, which represents the relative fraction of temperature variations linked to heating by star-forming regions; η is equivalent to $1 - E_{SF}/E_{Tot}$. Most of the η values from both studies are within ∼0.15, which is within the

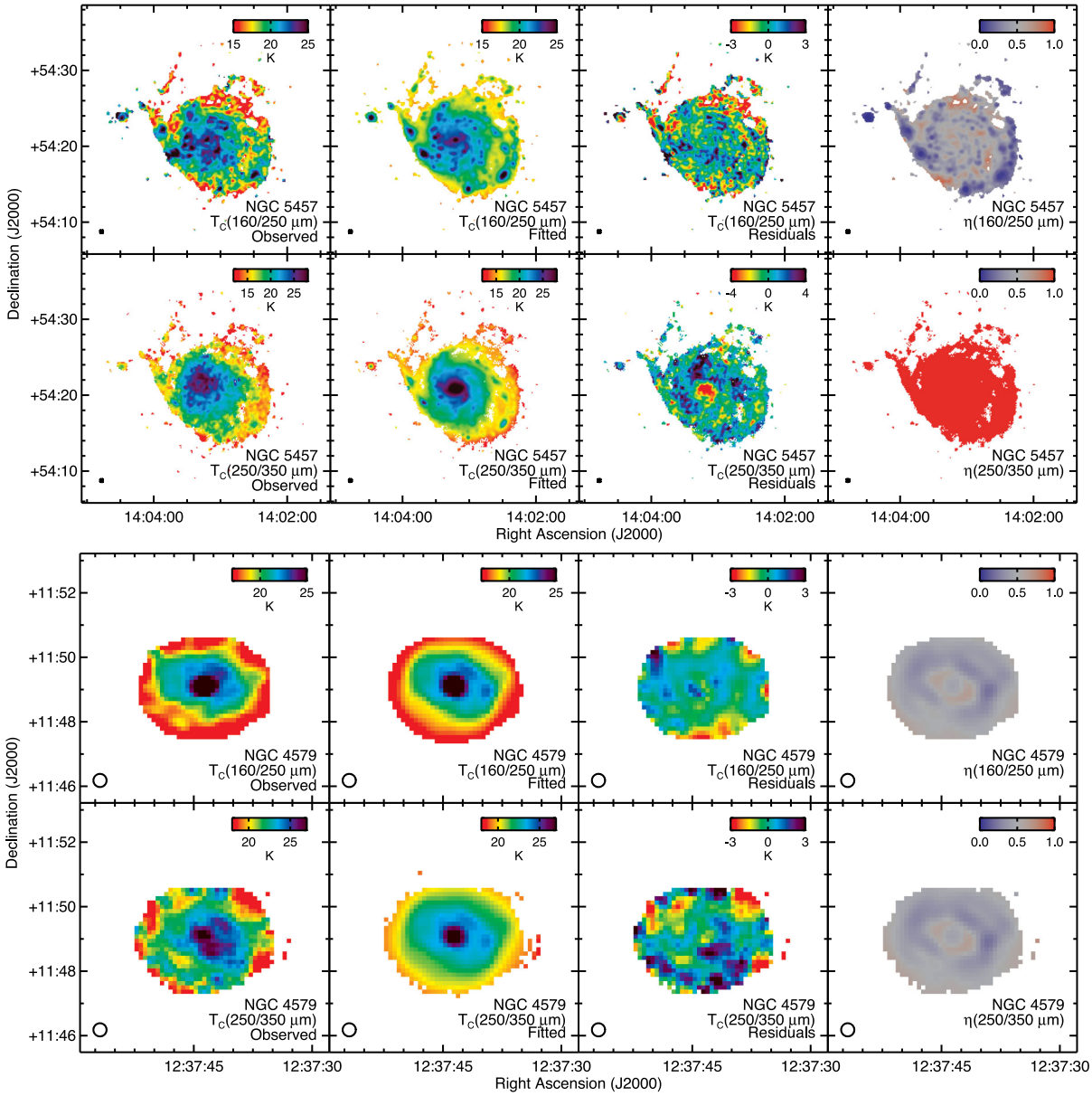

Figure 7. Examples of the results from using equation (2) to fit the 160/250 and 250/350 μm surface brightness ratios as a function of both the Hα and 3.6 μm data. The first columns of images on the left show the observed colour temperatures. The second column of images show the colour temperatures produced by adding together the Hα and 3.6 μm images using equation (2) and the best-fitting parameters from Table 5. The third column shows the residuals from subtracting the fitted colour temperature map from the observed colour temperature map. The fourth column shows the fraction of dust heating by the evolved stellar populations as predicted by the parameters in Table 5 and equation (3). The same galaxies are used as were shown in Fig. 1. Equivalent images for the other galaxies in the sample are available online. The images are formatted in the same way as the colour temperature images in Fig. 1. Images for the other galaxies in our sample are shown in the online version of this figure.

range of uncertainty of our methodology stated in Appendix G. The η(250/350 μm) measured in our new analysis for NGC 5236 is ∼0.30 higher than the value from Bendo et al. (2012a), which affects our interpretation of the dust heating. The 250/350 μm colour temperature map also includes significant structures (which may be either artefacts of the data processing or structures in the galaxy) that were not accurately fitted in the analysis, and both the extinction-corrected Hα and 3.6 μm maps trace similar spiral structures in NGC 5236, so it is possible that the uncertainties in the η values for this galaxy are much higher than our assumed uncertainty of 0.15. The results are also potentially affected by multiple other changes in the analysis, including the use of updated 160–350 μm data, the use of different tracers of dust heating sources, and changes in the angular resolution used in the analysis.

To check how distance-related effects could bias the results, we compared the η values obtained in 24 and 120 arcsec binned data in NGC 3031 and 5457, which simulates how the results would vary if the distance to the galaxies changed by a factor of 5. In this comparison, which is described in Appendix F, we found that the η values decrease somewhat in the 120 arcsec binned data but that the decrease was consistent with the uncertainties from the Monte Carlo analysis and the uncertainty of 0.15 in the methodology as described in Appendix G. We recommend treating the comparison of nearby galaxies to distant galaxies with some caution, but the

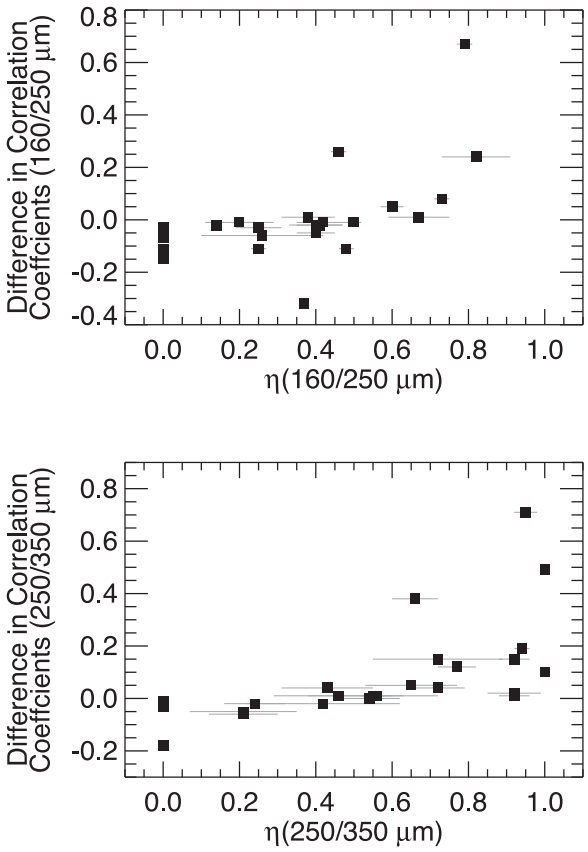

Figure 8. The *y*-axes show the difference between correlation coefficients in Table 4. For a given infrared surface brightness ratio, the correlation coefficient for the relation to Hα emission is subtracted from the coefficient for the relation to 3.6 μm emission. Positive values in the difference correspond to galaxies where variations in the infrared surface brightness ratio are more dependent on emission from the evolved stellar population, while negative values correspond to galaxies where the ratios primarily depend on emission from star-forming regions. The *x*-axes show the η values from Table 5 for the corresponding infrared surface brightness ratio, with higher values corresponding to more dust heating by older stars at the shorter wavelength in the ratio.

derived η values should not be so severely biased that they are unusable.

In yet another check of the analysis, we also found that the η values from Table 5 are consistent with the results from comparing the 160/250 and 250/350 μm ratios to the emission from Hα (or 24 μm emission) and 3.6 μm emission in Section 5. When $\eta > 0.70$, we typically find that the corresponding ratio is significantly better correlated with 3.6 μm emission, and when $\eta > 0.30$, we typically find that the corresponding ratio is better correlated with star formation. We do frequently find individual cases where one of the analyses produces less definitive results than the other, and the analyses sometimes produce correspondingly indeterminate results, but we do not have any example where the η values and the Section 5 analysis identify different dominant heating sources. Fig. 8 shows a comparison between η and the difference between the correlation coefficients from Table 4 for a given infrared surface brightness ratio. The correlation coefficient differences are based on subtracting the coefficient for the relation based on Hα emission from the coefficients for the relations based on 3.6 μm emission; higher values correspond to a higher fraction of the dust heating being attributed to the evolved stellar population. The relations are non-linear, but the data do show a trend. The Spearman correlation coefficients (which are more useful than Pearson correlation coefficients when assessing whether a non-linear trend is present) are 0.70 for the relation in the 160/250 μm data in Fig. 8 and 0.85 for the relation in the 250/350 μm data, indicating a good correspondence between η and the difference between the coefficients in Table 4. Overall, these results demonstrate that the dust heating sources identified using the η values derived in this section should generally be consistent with the analysis in Section 5.

6.1 Residual structures

The residual temperature structure maps can reveal issues with the quality of the fits. Some of the fits are quite good; the replicated colour temperatures match the observed colour temperatures to within 2–3 K. In quite a few galaxies, however, we see structures in the residual maps that are potentially imaging artefacts that would not be readily apparent when looking at the individual infrared images. Two of the most egregious examples of this are the 250/350 μm images for NGC 4548 and 5236, which, as also discussed above, have residual asymmetric structures that align with the scan direction of the SPIRE instrument. We also see a few regions where the residual images, particularly the 250/350 μm images, exhibit asymmetric hot or cold structures that cannot be easily replicated using equation (2). As mentioned previously, the 250/350 μm data for NGC 6946 exhibit the most severe artefacts, but we see similar notable artefacts in the 250/350 μm data for NGC 628, 3184, 4254, and 4736. These may be imaging artefacts, colour variations related to foreground cirrus structures, or real temperature structures produced by non-local dust heating effects, but in any case, the η(250/350 μm) derived here may not be reliable for some of these galaxies. Additionally, some of the residual temperature structure may look particularly pronounced because of the high dynamic range of the 160/250 or 250/350 μm data, which could be the case for NGC 3031 and 4736.

NGC 628, 3031, 4321, 4725, 4736, 5457, and 6946 all exhibit nuclei that appear unusually cold in the 250/350 μm residual maps, and the nucleus of NGC 6946 also appears cold in the map of the 160/250 μm data. This could arise for a few reasons. The fits to the NGC 628, 4736, and 6946 250/350 μm data were already flagged as problematic, and asymmetric dust temperature structures may have contributed to the appearance of the cold nuclei in these galaxies. NGC 3031, 4321, and 4725 have AGN (Ho, Filippenko & Sargent 1997; Moustakas et al. 2010) that can potentially produce synchrotron emission at submillimetre wavelengths that would make the colour temperatures appear colder. Moreover, in NGC 3031 and 4725, the synchrotron emission could appear relatively bright compared to the thermal emission from the dust because the surface density of the dust near the centres of these galaxies is relatively low compared to areas in the outer disc. The data in Fig. 7 clearly show that the 250/350 μm ratio is unusually suppressed for NGC 3031, but the results are not as clear for NGC 4725. It would also be unlikely that non-thermal AGN emission would explain the cold residuals in NGC 628, 5457, and 6946, which have optical nuclei spectra classified as star forming (Ho et al. 1997; Moustakas et al. 2010). Another possibility is that, when we use the 3.6 μm emission as a tracer of starlight from the evolved stellar population, the cold residuals appear because we are not removing emission from the bulge stars outside the planes of the target galaxies that is not heating the dust within the plane of the galaxies. As a result, when we recreate the colour temperature maps using the 3.6 μm, Hα, and 24 μm data, the bulge appears warmer in the fitted map than in the

observed map. This would satisfactorily explain the appearance of the cold nuclear residuals in galaxies with large bulges like NGC 4725 and 4736, but it is less clear that it explains why these residuals nuclear features appear in galaxies with small bulges like NGC 628, 5457, and 6946. A final possibility is that the relation of dust to its heating sources differs between the nuclei and discs in some galaxies, which is related to the hypothesis from Sauvage et al. (2010) stating that the infrared emission from these two galaxy components may be decoupled (see also Roussel et al. 2001). Ultimately, some combination of the above physical and analytical issues may be responsible for the appearance of the cold nuclear regions in the residual maps.

We also sometimes see hot spiral structures offset from spiral arms in a few galaxies, most notably in the 160/250 μm maps for NGC 628, 5236, and 6946. As discussed in Appendix E, this potentially appears because the dust around the star-forming regions in these structures is distributed asymmetrically, which then leads to asymmetries in how light from star-forming regions propagates into the ISM and heats the dust.

6.2 Relations between η and other galaxy properties

We looked at the relations between the η values and various other galaxy properties including morphological type, distance, inclination, luminosities, surface brightnesses, and luminosity ratios based on Hα, 3.6 μm, 24 μm, 160 μm, 250 μm, 350 μm, and 500 μm data (and including metrics related to star formation rates, specific star formation rates, stellar mass, dust mass, dust temperature, and dust obscuration), but we found no clear dependence of η on any global galaxy property. At best, we can only make a couple of tentative statements about the possible influence of various galaxy properties on η.

We did find that η was relatively high in NGC 3031 and 4736, two of the three Sab galaxies in this analysis. This could be because of the increased role that the large bulges play in dust heating in these galaxies, as also found by Sauvage & Thuan (1992) and Engelbracht et al. (2010). However, the η values for NGC 4725 are not as high as for the other two Sab galaxies, and some of the Sb-Sd galaxies have η values that are just as high as the values for NGC 3031 and 4736. Secondly, we found weak trends in which η(160/250 μm) decreases as the monochromatic luminosities measured in each of the 24–350 μm bands increase. However, the strongest relation (between η(160/250 μm) and the 160 μm luminosity) had a Spearman correlation coefficient with an absolute value of only 0.75, and the relations with infrared luminosities in other bands had coefficients of ∼0.70, which would imply that $\lesssim$50 per cent of the variance in η(160/250 μm) depends upon infrared luminosity. It is also unclear why the correlation coefficients for corresponding η(250/350 μm) are <0.50, which would indicate that η(250/350 μm) shows no significant relation to infrared luminosity.

We also found a slight bias in η(250/350 μm) with distance. The Spearman correlation coefficient for this relation is −0.63, which is relatively weak. However, η(250/350 μm) > 0.90 for most galaxies within distances of 7 Mpc but not for galaxies at larger distances. As explained in Appendix F, this could be because diffuse dust is more easily separated from star-forming regions in data with higher angular resolutions (see also Galliano et al. 2011), but the results from Appendix F show that we will still obtain η(250/350 μm) > 0.90 for sources like NGC 5457 at distances greater than 15 Mpc. It is also unclear why this effect is not seen for η(160/250 μm), where the corresponding correlation coefficient is −0.15. The other possibility is that, because of selection effects, we are seeing different forms of dust heating in nearby and distant galaxies, which is quite likely given the inhomogeneity of the sample. Many of the galaxies within 5 Mpc would not be selected for this analysis if they were at 20 Mpc simply because their angular sizes would be too small; it is plausible that dust heating in these galaxies may be different from the dust heating seen in the physically larger galaxies at larger distances.

Given the weakness of these trends, the relatively small and inhomogeneous nature of our sample, and some of the issues with our derivation of η (including how the η values depend on the star formation tracer used in the computation and potential biases in η with distance), we suggest to be extremely cautious regarding any of these trends in η. Further analyses with larger, homogeneous samples of galaxies or with better measurements of the fractions of dust heated by different sources may produce more reliable results.

7 DISCUSSION

7.1 Implications for dust modelling and SED fitting

We have identified far-infrared emission from multiple nearby galaxies produced by dust heated by intermediate-aged and older stars. What is surprising, however, is that we also find some galaxies where the far-infrared emission at $\leq$250 μm and possibly at longer wavelengths is mainly from dust heated by star-forming regions. Previously published results had implied that the transition between emission from warmer dust heated by star formation and colder dust heated by evolved stars should fall within a relatively narrow wavelength range. Bendo et al. (2010, 2012a) and Boquien et al. (2011), who had used the same techniques applied here but who had studied only a limited number of galaxies, had suggested that the transition was 160–250 μm. Hughes et al. (2014) presented NGC 891 as an example of a spiral galaxy where, using the same techniques, star-forming regions could be identified as the heating source for the dust seen at wavelengths as long as 350 μm. However, it was unclear whether the results for NGC 891 were just a consequence of issues with applying these analysis techniques to an edge-on galaxy where emission is integrated along the line of sight. It is clear now that NGC 891 is not the only galaxy where dust at $\geq$250 μm may be heated by star-forming regions. The results from the Draine & Li (2007) models applied to multiple galaxies (e.g. by Draine et al. 2007; Aniano et al. 2012; Dale et al. 2012; Mentuch Cooper et al. 2012; Ciesla et al. 2014) had suggested that the transition was at 30–100 μm. Our results, which include several of the galaxies contained in these studies, show that this transition point is typically at longer wavelengths. Indeed, the results from some radiative transfer models (e.g. Law, Gordon & Misselt 2011; De Looze et al. 2012) have placed this transition point in a wavelength range that more closely matches our empirical results.

Many existing dust emission and radiative transfer models (e.g. such as those published by Silva et al. 1998; Draine & Li 2007; Bianchi 2008; da Cunha et al. 2008; Baes et al. 2011; Popescu et al. 2011; Domínguez-Tenreiro et al. 2014) can accurately reproduce either globally integrated infrared galaxy SEDs or the SEDs of individual subregions within galaxies. To accurately characterize the dust emission, however, these models should also account for the broad variation in the transition wavelength between the two different dust components that we have identified. If the transition is at a wavelength that is too short, it could lead to dust temperatures that are too high and dust masses that are too low, while the converse would occur if the transition is at too long a wavelength.

In future research, we will examine either using existing models or developing new models to replicate not only the global SEDs of these galaxies but also the observed infrared surface brightness

ratio variations within them. For now, we can at least examine the implications of using single modified blackbody functions to estimate global dust temperature and mass.

Bendo et al. (2010) had proposed a method of fitting a single modified blackbody to the SED of M81 in which the function was fitted to the 160–500 μm data points and the 70 μm data point was treated as an upper limit. This is still appropriate for M81 because the emission in the full 160–500 μm range mostly originates from dust heated by the radiation field from the evolved stellar population. It may also be appropriate for galaxies where the dust is primarily heated by a single source, which could be either the evolved stellar population or star-forming regions [as in NGC 4254, 4303, 4501, and 5364 in this paper or as in NGC 891 as reported by Hughes et al. (2014)]. Based on the analysis from Bianchi (2013), the dust mass estimated from the modified blackbody fit will be accurate as long as the fitted data do not include emission from stochastically heated dust grains and do not sample regions with widely varying large grain dust temperatures [but also note the potential issues with resolution-related effects discussed by Galliano et al. (2011)] or major variations in other dust grain properties. However, our results show that, in a significant fraction of galaxies, the emission in the 160–350 μm range originates from dust heated by both star-forming regions and the evolved stellar population. In a few of these galaxies, the star-forming regions and the evolved stellar population appear to contribute equally to heating the emission at all wavelengths in this range; the single thermal components may still produce reasonable dust mass estimates in these cases, although this would depend on whether the large dust grains are close to the same temperature. In other galaxies, the dust observed at 160 μm is heated much more by star-forming regions than the dust observed at 350 μm. It is these cases where the single modified blackbodies fitted to the 160–500 μm data will yield the most inaccurate dust masses.

To examine how the dust temperatures and masses change if we divide the dust SED into different components based on the dust heating sources, we performed SED fits to the 160–500 μm data for NGC 628, 2403, and 5457, three galaxies where, based on our results, star-forming regions were responsible for ≥50 per cent of the heating for the dust seen at ≤160 μm but the evolved stellar populations were the dominant source of heating for the dust seen at ≥250 μm. Among the galaxies in the sample, the dust temperatures and masses from fits to the measured 160–500 μm data for these three galaxies should diverge the most from the quantities that would be found if we separated the SED into separate components based on the results from Section 6.

The global 70–500 μm flux densities that we use are given in Table 7. Because the PACS and SPIRE flux calibration have been recently updated, we needed to re-measure the flux densities; the measurements were made within apertures 1.5 times the size of the optical disc given by de Vaucouleurs et al. (1991, although this crosses the edges of the PACS images for NGC 5457). For NGC 2403, which was not observed at 100 μm with PACS, we used the 100 μm flux density from the *Infrared Astronomical Satellite* (*IRAS*) given by Rice et al. (1988). We also included MIPS 70 μm flux densities from Dale et al. (2009). Even though PACS 70 μm data were available, the MIPS 70 μm data have better signal-to-noise ratios and therefore seemed more trustworthy. Colour corrections and other photometric corrections have been applied to all PACS and SPIRE flux densities; colour corrections for *IRAS* and MIPS data are smaller than the uncertainties in the data and are therefore not applied.

To create SEDs representing separate warmer and colder components, we assumed for these three specific galaxies that all ≤100 μm emission originated from dust heated by star-forming regions and all ≥350 μm emission originated from dust heated by the evolved stellar population (although these are oversimplifications). The 160 μm data were multiplied by η(160/250 μm) and the 250 μm by η(250/350 μm) to get the emission at those wavelengths for the cold component, with the remainder assigned to the warm component. The uncertainties in the scaling terms are conservatively set at 0.15 based on the results from Appendix G.

We fit the data using the function

$$M_{\rm dust} = \frac{f_\nu D^2}{\kappa_\nu B_\nu(T)}, \quad (4)$$

which is a variant of the equation originally derived by Hildebrand (1983). In this equation, f_ν is the observed flux density, D is the distance, κ_ν is the dust opacity, and $B_\nu(T)$ is a blackbody function based on the temperature from the fits. We used κ_ν values based on interpolating in logarithm space between the tabulated values given by Draine (2003); for these κ_ν, β is equal to approximately (but not exactly) 2 in the 70–500 μm range. Although many *Herschel* results indicate that β may be between 1.5 and 2 (e.g. Boselli et al. 2012), it is unclear how to rescale the Draine (2003) opacities if $\beta \neq 2$, so we will not attempt using alternate values of β. We first perform fits to both the global 160–500 μm data in Table 6 and used the 70–100 μm flux densities as upper limits. We then fit the 70–250 μm data for the warm component and the 160–500 μm data for the cold components separately (excluding rescaled data where the measurements are $<3\sigma$). Note that the warm component is potentially emission from a sum of multiple thermal components and may not be accurately physically represented as a single modified blackbody, although the cold component can be physically approximated as a single modified blackbody (Bianchi 2013). The global SEDs for these galaxies as well as the separate rescaled components and best-fitting modified blackbodies functions are shown in Fig. 9. The resulting temperatures and masses are listed in Table 7.

The resulting temperatures change by 2–4 K between the unscaled data and rescaled cold component, which is higher than implied by the uncertainties. This change in temperature is small compared to the dust temperature variations seen in modified blackbodies fitted to 160–500 μm data (or similar wavelength ranges) for large samples of nearby galaxies, such as those studied by Galametz et al. (2012) and Cortese et al. (2014), but the resulting dust temperatures for the rescaled cold components are lower than what is obtained by these authors, even when they used the same emissivity functions. While the temperatures obtained by these authors are characteristic of the colours, they probably do not represent the actual dust temperatures of the coldest dust heated by the evolved stellar population in galaxies like NGC 628, 2403, and 5457. The actual variance in dust temperatures in nearby galaxies may therefore be higher than implied by the fits to 100–500 μm data.

The estimated masses for the rescaled cold component are not well defined, and the estimates are $<3\sigma$ for NGC 628. None the less, the results show that the dust masses may change by up to a factor of 2 between the unscaled and rescaled data. Gas-to-dust ratios obtained using dust masses from unscaled 160–500 μm data will tend to be high but still close enough to assess whether the gas-to-dust ratios are similar to the nominally expected values of 100–200 or whether dust masses appear unusually low relative to gas masses, as would be expected in low-metallicity regions. The data may exhibit more scatter if dust masses in some but not all of the galaxies are underestimated through fits to unscaled 160–500 μm data, although this increase scatter may not be significant in logarithm space.

Table 6. Measured and rescaled SEDs for NGC 628, 2403, and NGC 5457.

Galaxy	Wavelength (μm)	Measured flux density (Jy)[a]	Scaling factor (cold component)[b]	Rescaled flux densities (Jy) Warm component	Cold component
NGC 628	70	34 ± 4	0	34 ± 4	0
	100	83 ± 7	0	83 ± 7	0
	160	115 ± 10	0.25 ± 0.15	86 ± 19	29 ± 17
	250	65 ± 3	0.77 ± 0.15	15 ± 10	50 ± 10
	350	31.3 ± 1.3	1	0	31.3 ± 1.3
	500	12.8 ± 0.5	1	0	12.8 ± 0.5
NGC 2403	70	86 ± 10	0	86 ± 10	0
	100	150 ± 20	0	150 ± 20	0
	160	210 ± 20	0.48 ± 0.15	110 ± 30	100 ± 30
	250	129 ± 5	0.94 ± 0.15	8 ± 20	120 ± 20
	350	68 ± 3	1	0	68 ± 3
	500	29.3 ± 1.2	1	0	29.3 ± 1.2
NGC 5457	70	118 ± 14	0	118 ± 14	0
	100	250 ± 20	0	250 ± 20	0
	160	370 ± 30	0.37 ± 0.15	220 ± 60	150 ± 60
	250	208 ± 8	1	0	208 ± 8
	350	102 ± 4	1	0	102 ± 4
	500	42.4 ± 1.7	1	0	42.4 ± 1.7

Note: [a]All flux density measurements except the 60 μm measurements and the 100 μm measurement for NGC 2403 include colour corrections.
[b]See the text in Section 7.1 for how these numbers are set.

In addition to the issues described above, dust masses can potentially be underestimated from fitting modified blackbodies to SEDs in other ways. Emission at <100 μm potentially includes stochastically heated dust that will appear warmer than the larger dust grains that are in thermodynamic equilibrium with the illuminating radiation field; fitting a single modified blackbody to data from 60, 70, or possibly even 100 to 500 μm could produce temperatures that are warmer than the bulk of the dust grains and dust masses that are too low. Additionally, many authors allow β to vary as a free parameter in SED fits, but degeneracies between β and temperature (e.g. Shetty et al. 2009; Galametz et al. 2012; Kirkpatrick et al. 2014) could cause dust temperatures to generally appear warmer than the actual dust temperatures and thus make the dust masses appear lower. Moreover, <15 K dust visible only on the Rayleigh–Jeans side of the dust SED could make β appear lower than it actually is (Kirkpatrick et al. 2014), which not only gives the false appearance that β is variable among or within galaxies but also potentially leads to even lower dust masses.

As our analysis shows, it is somewhat difficult to use the η values from Section 6 to accurately rescale dust SEDs. Our SED fitting approach oversimplifies the physics of the dust emission and makes some relatively crude assumptions about the division between warm and cold thermal components. To measure more accurate dust masses within individual galaxies, we recommend not only using dust models with more realistic modelling of the dust heating and radiation but also performing fits with these models that replicate not only the observed flux densities but also the observed colour temperature variations within the galaxies. See De Looze et al. (2014) for an example of this approach.

7.2 Implications for measuring star formation rates

The results here also have implications for using infrared emission to measure star formation rates. A commonly held classical perspective has been that dust emission traces star formation because dust is primarily absorbing light from star-forming regions. This has generally been true for mid-infrared wavebands tracing hot dust, such as the *Spitzer* 24 μm or *WISE* 22 μm band. However, prior to our analysis, several different authors had presented multiple observational results implying that this did not apply to the far-infrared, including the demonstration that the ratio of far-infrared to Hα emission was higher in spiral galaxies with large bulges than in spiral galaxies with small bulges (Sauvage & Thuan 1992); the observation that the scatter in the ratio of far-infrared to Hα emission for subregions within galaxies was higher for longer infrared wavelengths than shorter wavelengths (Calzetti et al. 2010); and the prior *Herschel*-based analyses relating variations in the far-infrared surface brightness ratios to the evolved stellar population. Additionally, Boquien et al. (2011) and Bendo et al. (2012a) had demonstrated that far-infrared emission could still be correlated with other star formation tracers, such as Hα and 24 μm emission, even when variations in the infrared surface brightness ratios demonstrated that the dust was heated by the evolved stellar populations. Both authors suggested that these seemingly contradictory results could be valid if the dust heated by the evolved stellar population was tracing the gas that fuels star formation, which would be related to star formation through the Kennicutt–Schmidt law (Schmidt 1959; Kennicutt 1998). They also proposed a scenario where emission at shorter wavelengths originated from dust near young stars within star-forming regions that was optically thick to ultraviolet light while emission at longer wavelengths came from dust in outer shells that were shielded from the ultraviolet photons from the star-forming regions and that were therefore mainly heated by light from the older stellar population.

Our new results show that this scenario describing the relation of far-infrared dust emission to star formation is oversimplistic. In some cases, the far-infrared emission still appears related to star formation through the Kennicutt–Schmidt law, as the dust is primarily heated by the evolved stellar population, and the Boquien et al. (2011) and Bendo et al. (2012a) scenario of the structure of dust around star-forming regions still applies. In other galaxies, all of the dust is heated by the star-forming regions. Using far-infrared emission to trace star formation therefore becomes

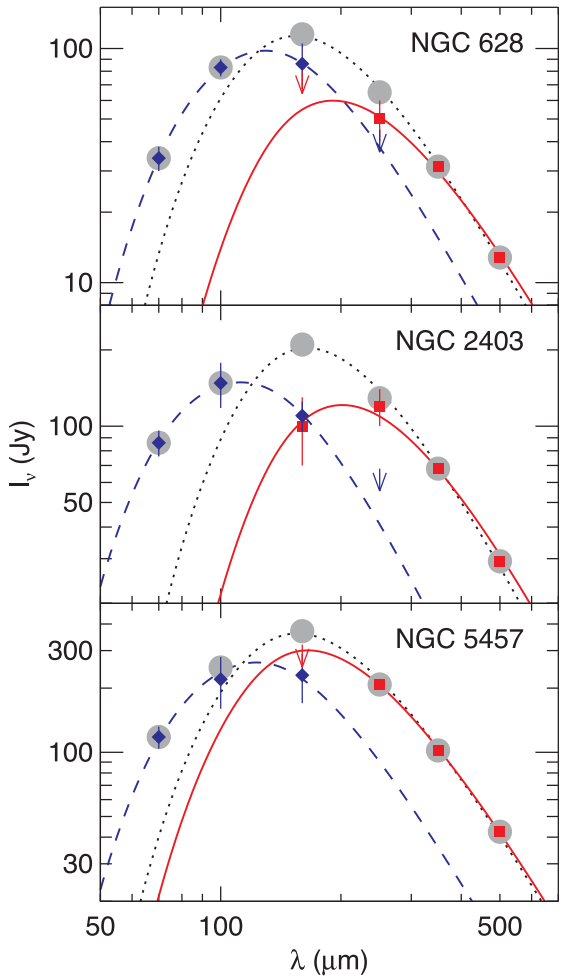

Figure 9. 70–500 μm SEDs for NGC 628, 2403, and 5457. The grey circles show the measured unscaled global flux densities for these galaxies. The blue diamonds show the rescaled data for the component of the SED from dust heated by star-forming regions, and the red squares show the component from dust heated by the evolved stellar population, both of which were found by rescaling the data using the results from Section 6. Flux densities which are not measured at the 3σ level are represented as arrows showing the 3σ upper limits; the upper limits were not used in the fits. These data and the rescaling factors are listed in Table 6. The black dotted line shows the best-fitting modified blackbody function for the measured global flux densities, and the blue dashed and red solid lines show the best-fitting function for the rescaled data. The emissivity function for the modified blackbody function is equivalent to the function for the tabulated κ_ν values given by Draine (2003), where β is approximately equal to 2. The dust temperatures and masses for the best-fitting functions are listed in Table 7.

problematic, as the functional relation between star formation rate and infrared emission changes in these two scenarios. In the case where far-infrared emission originates from dust heated directly by the star-forming regions, the relation between the emission and star formation rate should be linear. In the case where the emission is from dust not heated by star formation but tracing the fuel for star formation, the relation could be expected to follow a power law with an index of 1–2. If far-infrared emission is sometimes related to the star formation rate through direct dust heating by star-forming regions and sometimes related through the Kennicutt–Schmidt law, then we can expect the relation between the two quantities to exhibit significant scatter, especially when looking at longer wavelengths where more inconsistency is expected. In the cases where dust emission is related to star formation through the Kennicutt–Schmidt law, it should also be possible to see dust emission from locations that have not achieved the critical density for star formation described by Kennicutt (1998), and this will add scatter to the empirical relation between far-infrared emission and star formation. Kennicutt et al. (2009) pointed out that such diffuse dust emission can be seen at wavelengths as short as 24 μm, so dust emission unassociated with star formation would naturally be expected at longer wavelengths.

Several authors, including Calzetti et al. (2007), Leroy et al. (2008), Zhu et al. (2008), Kennicutt et al. (2009), Hao et al. (2011), and Lee et al. (2013), have developed star formation metrics based on combining measurements of ultraviolet or Hα emission (tracing the fraction of unextinguished light from star-forming regions) with infrared light (tracing the fraction of extinguished light from star-forming regions). This naturally works if the re-radiated light is from the dust heated by the star-forming regions. However, our analysis shows that far-infrared emission sometimes originates from dust heated by the intermediate-aged and older stars. Because of this, using far-infrared emission to correct ultraviolet or optical star formation tracers may potentially be inaccurate, although the far-infrared emission may still correlate well with the column density of dust obscuring star-forming regions and may therefore still be useful for extinction corrections. Most previously published extinction-corrected star formation metrics, however, rely either on mid-infrared dust emission or infrared emission integrated over a large wavelength range such as 3–1100 μm. Mid-infrared emission should mainly contain light from dust heated directly by star-forming regions, so that waveband should be relatively accurate for correcting for dust extinction. However, integrated infrared emission may include substantial emission from dust heated by older stars, especially in galaxies with low star formation rates or large spheroids of evolved stars, and therefore may provide an inaccurate extinction correction for ultraviolet and optical star formation tracers (see also De Looze et al. 2012).

8 CONCLUSIONS

In our analysis of variations in the 160/250 and 250/350 μm surface brightness ratios observed within 24 nearby galaxies, we have identified a broad variation in the heating of the dust observed in the 160–350 μm range. At one extreme, we definitively identified star-forming regions as the primary heating source for dust seen at $\leq$250 μm and possibly at longer wavelengths in at least four galaxies, and a fifth galaxy may also fall into this category. At the other extreme, we find strong evidence that emission at $\geq$160 μm and possibly shorter wavelengths originates from dust heated by the evolved stellar population in at least three galaxies, and weaker evidence suggests that two other galaxies may fall into this category. Among the rest of the galaxies, we either see a transition from observing dust heated by star formation at 160 μm to observing dust heated by the evolved stellar population at 350 μm or see 160–350 μm emission from dust heated by a mixture of young and old stars.

In Table 8, we list summaries of what we have identified as the heating sources that influence the 160/250 and 250/350 μm ratios for each galaxy based on the results from the analyses in Sections 4–6. We identify definite heating sources for galaxies and ratios where the analyses from at least two of the three sections show that the ratios depend primarily on one heating source. We mark cases as questionable when one of the quantitative analyses suggests a predominant heating source influencing a ratio but when

Table 7. Dust temperatures and masses for NGC 628, 2403, and 5457.

Galaxy	Unscaled data		Rescaled data			
			Warm component		Cold component	
	Dust temperature (K)	Dust mass ($M_\odot$)	Dust temperature (K)	Dust mass ($M_\odot$)	Temperature (K)	Mass ($M_\odot$)
NGC 628	18.2 ± 0.6	$(7.2 \pm 0.7) \times 10^7$	22.5 ± 1.3	$(2.1 \pm 0.8) \times 10^7$	14.5 ± 1.8	$(1.3 \pm 0.5) \times 10^8$
NGC 2403	16.9 ± 0.5	$(2.0 \pm 0.2) \times 10^7$	26.1 ± 1.1	$(1.6 \pm 0.4) \times 10^6$	13.7 ± 1.0	$(3.5 \pm 1.0) \times 10^7$
NGC 5457	18.1 ± 0.6	$(1.1 \pm 0.1) \times 10^8$	23.8 ± 1.7	$(2.0 \pm 0.8) \times 10^7$	16.8 ± 0.6	$(1.3 \pm 0.1) \times 10^8$

Table 8. Summary of identified dust heating sources related to surface brightness ratios.

Galaxy	Heating source[a]	
	160/250 μm	250/350 μm
NGC 628	SF	ES
NGC 925	SF	Mixed
NGC 2403	SF	ES
NGC 3031	ES	ES
NGC 3184	Mixed	ES?
NGC 3621	ES	ES[b]
NGC 3631	Mixed	Mixed
NGC 3938	SF	Mixed
NGC 3953	Mixed	ES
NGC 4254	SF	SF
NGC 4303	SF	SF
NGC 4321	SF?	SF?
NGC 4501	SF	SF
NGC 4535	Mixed	ES?
NGC 4548	ES	ES[b]
NGC 4579	Mixed	Mixed
NGC 4725	ES?	ES?
NGC 4736	Mixed	ES
NGC 5055	SF	Mixed[c]
NGC 5236	SF	ES?
NGC 5364	SF	SF
NGC 5457	SF	ES
NGC 6946	SF?	[d]
NGC 7793	ES?	ES

Note: [a]SF stands for star formation. ES stands for the evolved stellar population. Mixed indicates that both of these sources may heat the dust equally or that the results are ambiguous. Question marks are placed next to the cases where only one of the quantitative analyses identified this as the heating source and the other analyses produced ambiguous results.

[b]The results for the 160/250 μm data strongly indicated dust heating by the evolved stellar population at those wavelengths, but the results from the 250/350 μm data were more indeterminate. In these cases, it seems more likely in these cases that the 250/350 μm is also linked to the evolved stellar population.

[c]The qualitative appearance of the 250/350 μm colour temperature map does not match what is predicted by some of the quantitative results, so we labelled this as mixed.

[d]The 250/350 μm colour temperature structures for this galaxy cannot be straightforwardly related to any dust heating source.

the results from the other quantitative analysis and the qualitative analysis of the colour temperature maps provide ambiguous results. Other galaxies and ratio are marked as mixed. These mixed cases are often situations where the 160/250 or 250/350 μm ratios are influenced equally by star-forming regions and the evolved stellar population or the cases where the structures traced by both heating sources are so similar that the colour temperatures appear to be equally related to both. We also highlight a number of cases where the analysis produced confusing or illogical results as well as the confusing results for NGC 6946, where the 250/350 μm colour temperature map did not look related to any dust heating source.

We were unable to link any individual galaxy property to the dust heating mechanisms. We found that dust tended to be heated more by the evolved stellar population in the Sab galaxies than in the Sb-Sd galaxies but that dust tended to be heated by star-forming regions more in galaxies with high infrared surface brightnesses. However, the evidence for all of this is statistically weak because of the limited sample size used and because of the limited work that could be done with our analysis results.

None the less, our results demonstrate a substantial variation in the relative magnitudes of the emission from warmer dust heated by star-forming regions and colder dust heated by the evolved stellar populations within galaxies and a substantial variation in the wavelength marking the transition point between emission from warmer and colder thermal components. SED fitting performed with either modified blackbodies or more complex dust emission or radiative transfer models should be able to account for or replicate these variations to more accurately measure dust temperatures and masses. These functions and models are typically fitted to observed flux densities or surface brightnesses and often match the magnitudes of the flux densities very well. It would be interesting to test whether these fits can accurately replicate the colours of these objects (effectively the derivative of the SED curve), including the variations in infrared surface brightness ratios that we displayed in Fig. 1. Additionally, it would be appropriate to either build new dust emission or radiative transfer models or adjust existing models so that they can replicate these colour variations as well as the magnitudes of the global and local SEDs.

ACKNOWLEDGEMENTS

We thank the reviewer for the helpful comments on this paper. GJB is funded by the STFC. IDL is a postdoctoral researcher of the FWO-Vlaanderen (Belgium). The *Herschel* spacecraft was designed, built, tested, and launched under a contract to ESA managed by the *Herschel*/*Planck* Project team by an industrial consortium under the overall responsibility of the prime contractor Thales Alenia Space (Cannes), and including Astrium (Friedrichshafen) responsible for the payload module and for system testing at spacecraft level, Thales Alenia Space (Turin) responsible for the service module, and Astrium (Toulouse) responsible for the telescope, with in

excess of a hundred subcontractors. SPIRE has been developed by a consortium of institutes led by Cardiff University (UK) and including Univ. Lethbridge (Canada); NAOC (China); CEA, LAM (France); IFSI, Univ. Padua (Italy); IAC (Spain); Stockholm Observatory (Sweden); Imperial College London, RAL, UCL-MSSL, UKATC, Univ. Sussex (UK); and Caltech, JPL, NHSC, Univ. Colorado (USA). This development has been supported by national funding agencies: CSA (Canada); NAOC (China); CEA, CNES, CNRS (France); ASI (Italy); MCINN (Spain); SNSB (Sweden); STFC, UKSA (UK); and NASA (USA). HIPE is a joint development (are joint developments) by the *Herschel* Science Ground Segment Consortium, consisting of ESA, the NASA *Herschel* Science Center, and the HIFI, PACS and SPIRE consortia. This publication makes use of data products from the *Wide-field Infrared Survey Explorer*, which is a joint project of the University of California, Los Angeles, and the Jet Propulsion Laboratory/California Institute of Technology, funded by the National Aeronautics and Space Administration. This research has made use of the NASA/IPAC Extragalactic Database (NED) which is operated by the Jet Propulsion Laboratory, California Institute of Technology, under contract with the National Aeronautics and Space Administration.

REFERENCES

Altieri B., Vavrek R., eds, 2013, PACS Observer's Manual, Version 2.5.1. Herschel Science Centre, Villanueva de la Cañada, Madrid
Amanullah R. et al., 2010, ApJ, 716, 712
Aniano G., Draine B. T., Gordon K. D., Sandstrom K., 2011, PASP, 123, 1218
Aniano G. et al., 2012, ApJ, 756, 138
Auld R. et al., 2013, MNRAS, 428, 1880
Baes M., Verstappen J., De Looze I., Fritz J., Saftly W., Vidal Pérez E., Stalevski M., Valcke S., 2011, ApJS, 196, 22
Bendo G. J. et al., 2007, MNRAS, 380, 1313
Bendo G. J. et al., 2010, A&A, 518, L65
Bendo G. J. et al., 2012a, MNRAS, 419, 1833
Bendo G. J., Galliano F., Madden S. C., 2012b, MNRAS, 423, 197
Bendo G. J. et al., 2013, MNRAS, 433, 3062
Bianchi S., 2007, A&A, 471, 765
Bianchi S., 2008, A&A, 490, 461
Bianchi S., 2013, A&A, 552, 89
Boquien M. et al., 2011, AJ, 142, 111
Boselli A., Gavazzi G., 2002, A&A, 386, 124
Boselli A. et al., 2010, PASP, 122, 261
Boselli A. et al., 2012, A&A, 540, 54
Boselli A., Hughes T. M., Cortese L., Gavazzi G., Buat V., 2013, A&A, 550, 114
Calzetti D. et al., 2005, ApJ, 633, 871
Calzetti D. et al., 2007, ApJ, 666, 870
Calzetti D. et al., 2010, ApJ, 714, 1256
Ciesla L. et al., 2014, A&A, 565, 128
Cortese L. et al., 2014, MNRAS, 440, 942
Cutri R. M. et al., 2013, Explanatory Supplement to the WISE All-Sky Data Release Products. IPAC, Pasadena
da Cunha E., Charlot S., Elbaz D., 2008, MNRAS, 388, 1595
Dale D. A. et al., 2007, ApJ, 655, 863
Dale D. A. et al., 2009, ApJ, 703, 517
Dale D. A. et al., 2012, ApJ, 745, 95
Davies J. I. et al., 2010, MNRAS, 518, L48
Davies J. I. et al., 2012, MNRAS, 419, 3505
de Vaucouleurs G., de Vaucouleurs A., Corwin H. G., Buta R. J., Paturel G., Fouque P., 1991, Third Reference Catalogue of Bright Galaxies. Springer-Verlag, Berlin
De Looze I. et al., 2012, MNRAS, 427, 2797
De Looze I. et al., 2014, preprint (arXiv:1409.3857)
Dessart L. et al., 2008, ApJ, 675, 644
Dobbs C. L., Pringle J. E., 2010, MNRAS, 409, 396
Domínguez-Tenreiro R., Obreja A., Granato G. L., Schurer A., Alpresa P., Silva L., Brook C. B., Serna A., 2014, MNRAS, 439, 3868
Draine B. T., 2003, ARA&A, 41, 241
Draine B. T., Li A., 2007, ApJ, 657, 810
Draine B. T. et al., 2007, ApJ, 663, 866
Elmegreeen B. G., 1979, ApJ, 231, 372
Engelbracht C. W. et al., 2007, PASP, 119, 994
Engelbracht C. W. et al., 2010, A&A, 518, L56
Foyle K. et al., 2012, MNRAS, 421, 2917
Freedman W. L. et al., 2001, ApJ, 553, 47
Galametz M. et al., 2010, A&A, 518, L55
Galametz M. et al., 2012, MNRAS, 425, 763
Galliano F. et al., 2011, A&A, 536, 88
Griffin M. J. et al., 2010, A&A, 518, L3
Groves B. et al., 2012, MNRAS, 426, 892
Hao C.-N., Kennicutt R. C., Jr, Johnson B. D., Calzetti D., Dale D. A., Moustakas J., 2011, ApJ, 741, 124
Helou G. et al., 2004, ApJS, 154, 253
Hildebrand R. H., 1983, QJRAS, 24, 267
Ho L., Filippenko A. V., Sargent W. L. W., 1997, ApJS, 112, 315
Hoopes C. G., Walterbos R. A. M., Bothun G. D., 2001, ApJS, 559, 878
Hughes T. M. et al., 2014, A&A, 565, 4
IRAC Instrument and Instrument Support Teams, 2013, IRAC Instrument Handbook, Version 2.0.3. Spitzer Science Center, Pasadena
Jarrett T. H., Chester T., Cutri R., Schneider S. E., Huchra J. P., 2003, AJ, 125, 525
Kennicutt R. C., Jr, 1998, ApJ, 498, 541
Kennicutt R. C., Jr et al., 2003, PASP, 115, 928
Kennicutt R. C., Jr, Lee J. C., Funes J. G. S. J., Sakai S., Akiyama S., 2008, ApJS, 178, 247
Kennicutt R. C., Jr et al., 2009, ApJ, 703, 1672
Kennicutt R. C., Jr et al., 2011, PASP, 123, 1347
Kirkpatrick A. et al., 2014, ApJ, 789, 130
Kroupa P., 2001, MNRAS, 322, 231
Law K.-H., Gordon K. D., Misselt K. A., 2011, ApJ, 738, 124
Lee J. C., Hwang H. S., Ko J., 2013, ApJ, 774, 62
Leitherer C. et al., 1999, ApJS, 123, 3
Leroy A. K., Walter F., Brinks E., Bigiel F., de Blok W. J. G., Madore B., Thornley M. D., 2008, AJ, 136, 2782
Lu N. et al., 2003, ApJ, 588, 199
Lutz D., 2012, PACS Photometer Point Spread Function, Version 2.0. Herschel Science Centre, Villanueva de la Cañada, Madrid
Meidt S. E. et al., 2012, ApJ, 744, 17
Mentuch Cooper E. et al., 2012, ApJ, 755, 165
Mentuch E. et al., 2009, ApJ, 706, 1020
Mentuch E., Abraham R. G., Zibetti S., 2010, ApJ, 725, 1971
Meurer G. R. et al., 2006, ApJS, 165, 307
Misiriotis A., Popescu C. C., Tuffs R., Kylafis N. D., 2001, A&A, 372, 775
Moustakas J., Kennicutt R. C., Jr, Tremonti C. A., Dale D. A., Smith J.-D. T., Calzetti D., 2010, ApJS, 190, 233
Müller T., Okumura K., Klaas U., 2011, PACS Photometer Passbands and Colour Correction Factors for Various Source SEDs, Version 1.0. Herschel Science Centre, Villanueva de la Cañada, Madrid
Muñoz-Mateos J. C. et al., 2009, ApJ, 703, 1569
Olivares E. et al., 2010, ApJ, 715, 833
Ott S., 2010, in Mizumoto Y., ed., ASP Conf. Ser. Vol. 434, Astronomical Data Analysis Software and Systems XIX. Astron. Soc. Pac., San Francisco, p. 139
Pietrzynski G. et al., 2010, AJ, 140, 1475
Pilbratt G. et al., 2010, A&A, 518, L1
Planck Collaboration XIX, 2011, A&A, 536, A19
Planck Collaboration XXV, 2014, preprint (arXiv:1407.5452)
Poglitsch A. et al., 2010, A&A, 518, L2
Popescu C. C., Tuffs R. J., Dopita M. A., Fischera J., Kylafis N. D., Madore B. F., 2011, A&A, 527, A109
Poznanski D. et al., 2009, ApJ, 694, 1067
Pozzi F., Di Matteo T., Aste T., 2012, Eur. Phys. J. B., 85, 175

Prescott M. K. M. et al., 2007, ApJ, 668, 182
Rice W., Lonsdale C. J., Soifer B. T., Neugebauer G., Kopan E. L., Lloyd L. A., de Jong T., Habing H. J., 1988, ApJS, 68, 91
Rieke G. H. et al., 2004, ApJS, 154, 25
Roberts W. W., 1969, ApJ, 158, 123
Roussel H., 2013, PASP, 125, 1126
Roussel H. et al., 2001, A&A, 372, 406
Rowan-Robinson M. et al., 2010, MNRAS, 409, 2
Roy R. et al., 2011, ApJ, 736, 76
Saha A., Thim F., Tammann G. A., Reindl B., Sandage A., 2006, ApJS, 165, 108
Sauvage M., Thuan T. X., 1992, ApJ, 396, L69
Sauvage M. et al., 2010, A&A, 518, L64
Schlafly E. F., Finkbeiner D. P., 2011, ApJ, 737, 103
Schmidt M., 1959, ApJ, 129, 243
Sheth K. et al., 2010, PASP, 122, 1397
Shetty R., Kauffman J., Schnee S., Goodman A. A., Ercolano B., 2009, ApJ, 696, 2234
Silva L., Granato G. L., Bressan A., Danese L., 1998, ApJ, 509, 103
Smith M. W. L., 2012, PhD thesis, Cardiff University
Smith M. W. L. et al., 2010, A&A, 518, L51
Smith M. W. L. et al., 2012a, ApJ, 748, 123
Smith M. W. L. et al., 2012b, ApJ, 756, 40
Spitzer Science User Support and Instrument Teams, IRSA Science User Support Team, 2012, Spitzer Data Analysis Cookbook, Version 5.0.1. Spitzer Science Center, Pasadena
Storey P. J., Zeippen C. J., 2000, MNRAS, 312, 813
Tabatabaei F. S. et al., 2014, A&A, 561, 95
Thereau G., Hanski M. O., Coudreau N., Hallet N., Martin J.-M., 2007, A&A, 465, 71
Tonry J. L., Dressler A., Blakeslee J. P., Ajhar E. A., Fletcher A. B., Luppino G. A., Metzger M. R., Moore C. B., 2001, ApJ, 546, 681
Tully R. B., Rizzi L., Shaya E. J., Courtois H. M., Makarov D. I., Jacobs B. A., 2009, AJ, 138, 323
Valtchanov I., ed., 2014, The Spectral and Photometric Imaging Receiver (SPIRE) Handbook, Version 2.5. *Herschel* Science Centre, Villanueva de la Cañada, Madrid
Werner M. W. et al., 2004, ApJS, 154, 1
Wright E. L. et al., 2010, AJ, 140, 1868
Xilouris E. M., Byun Y. I., Kylafis N. D., Paleologou E. V., Papamastorakis J., 1999, A&A, 344, 868
Xilouris E. M. et al., 2012, A&A, 543, 74
Zhu Y.-N., Wu H., Cao C., Li H.-N., 2008, ApJ, 686, 155

APPENDIX A: COMPARISONS OF Hα AND 24 μm EMISSION

Multiple authors (e.g. Calzetti et al. 2005, 2007; Prescott et al. 2007) have found a good correspondence between Hα and 24 μm emission from compact sources within nearby galaxies. However, it is possible for diffuse dust to produce 24 μm emission, and this diffuse emission will not necessarily correspond to Hα emission (Kennicutt et al. 2009). Additionally, the ratio of Hα to 24 μm emission may vary with metallicity as well. To examine whether this could affect our analysis, we compared uncorrected Hα and 24 μm emission measured within the 24 arcsec binned data in our analysis, as we also compared the correlations of the 160/250 and 250/350 μm ratios to the uncorrected Hα, corrected Hα, and 24 μm emission. We selected data for 24 arcsec bins where both the uncorrected Hα and 24 μm emission were measured at the 3σ level and where the data otherwise met the criteria for use in the analysis in Section 5; the data meeting the criteria for analysis on the 250/350 μm ratio were also used for calculating correlation coefficients for the relations between the uncorrected Hα and 24 μm emission. These selection criteria are necessary for directly comparing Hα and 24 μm emission but may cause the resulting coefficients to differ slightly (<0.05) from the coefficients in Table 4 listed for the same relations.

The weighted correlation coefficients from this analysis are presented in Table A1. First, we can see that while the uncorrected Hα and 24 μm data are often strongly correlated, the correlation coefficients do not always equal 1, and some of the values drop to <0.80. Although the Hα and 24 μm emission is clearly correlated, enough scatter exists that swapping one for the other could potentially change the relations we see when comparing these star formation tracers to the 160/250 and 250/350 μm surface brightness ratios. Further analysis to understand these variations and, in particular, to identify whether they are associated with other properties of the ISM (such as the gas-to-dust ratio or metallicity), would be useful, but this is beyond the scope of this paper.

In the comparison of the different star formation tracers to the infrared surface brightness ratios, we generally found that the correlations with the uncorrected Hα emission were the weakest and the correlations with the 24 μm emission were strongest. The correlation coefficients for the relations using the extinction-corrected Hα emission usually fell between the other two, which is expected given that the corrected Hα emission is based on a combination of the uncorrected Hα and 24 μm emission. The coefficients for the relations with the corrected Hα emission are sometimes higher than for the corresponding relations with the 24 μm emission, but with one exception (the relations for the 160/250 μm ratio for NGC 5364, where all coefficients are <0.50), the difference never exceeds 0.05.

For 15 of the 22 galaxies, the weighted correlation coefficients were ≥0.05 higher for at least one (but usually two) of the relations between the far-infrared ratios and the 24 μm surface brightness than for the corresponding relations between the ratios and the uncorrected Hα intensity. NGC 3031, 3953, 4548, and 4725 are all cases where we masked emission in the centres of the Hα image that we determined was incompletely subtracted continuum emission (based on the diffuse appearance of the emission and the presence of artefacts similar to what was seen for foreground stars). We did not remove any 24 μm emission from these regions, which probably originates from dust heated in part or completely by the evolved stellar population, particularly the bulge stars. If the emission at 160–350 μm also originates from dust heated by the evolved stellar population, then the 160/250 and 250/350 μm ratios may naturally correlate with the 24 μm band very well within these central regions, and the correlation coefficients for the overall relations between the far-infrared ratios and 24 μm emission will be higher than the relations between the ratios and the Hα emission. We therefore should disregard the 'improved' relation found between the ratios and the 24 μm emission in these four galaxies. Of the remaining 11 galaxies where a significantly stronger correlation is found between either ratio and 24 μm emission, the major question is whether changing the star formation tracer would alter our interpretation of whether the far-infrared ratios were more strongly affected by star-forming regions or the evolved stellar population as presented in Section 5. NGC 628, 925, 3184, 3938, 4303, 5364, and 7793 are the only remaining cases where this could be an issue. In these seven galaxies, we would be more likely to infer that dust heating by star-forming regions is less significant when using the uncorrected Hα emission or more significant when using the 24 μm emission. This may still be caused in part by 24 μm emission from dust heated by the diffuse ISRF.

Table A1. Results of using different star formation tracers in comparison to infrared surface brightness ratios.

Galaxy	Weighted correlation coefficients						
	$\log(I_\nu(24\ \mu m))$ versus $\log(I(H\alpha))$ (uncorrected)	$\log(I_\nu(160\ \mu m)/I_\nu(250\ \mu m))$ versus $\log(I(H\alpha))$ (uncorrected)	$\log(I_\nu(160\ \mu m)/I_\nu(250\ \mu m))$ versus $\log(I(H\alpha))$ (corrected)	$\log(I_\nu(160\ \mu m)/I_\nu(250\ \mu m))$ versus $\log(I_\nu(24\ \mu m))$	$\log(I_\nu(250\ \mu m)/I_\nu(350\ \mu m))$ versus $\log(I(H\alpha))$ (uncorrected)	$\log(I_\nu(250\ \mu m)/I_\nu(350\ \mu m))$ versus $\log(I(H\alpha))$ (corrected)	$\log(I_\nu(250\ \mu m)/I_\nu(350\ \mu m))$ versus $\log(I_\nu(24\ \mu m))$
NGC 628	0.86	0.73	0.82	0.83	0.57	0.72	0.76
NGC 925	0.92	0.81	0.82	0.84	0.86	0.88	0.91
NGC 2403	0.97	0.91	0.92	0.91	0.74	0.75	0.77
NGC 3031	0.93	0.40	0.47	0.55	0.29	0.36	0.48
NGC 3184	0.80	0.67	0.81	0.82	0.59	0.75	0.80
NGC 3621	0.94	0.84	0.87	0.90	0.87	0.89	0.90
NGC 3631	0.99	0.94	0.95	0.96	0.93	0.95	0.96
NGC 3938	0.95	0.92	0.96	0.97	0.84	0.88	0.90
NGC 3953	0.91	0.76	0.83	0.84	0.62	0.68	0.71
NGC 4254	0.98	0.89	0.88	0.87	0.68	0.69	0.70
NGC 4303	0.83	0.87	0.88	0.85	0.86	0.91	0.91
NGC 4321	1.00	0.97	0.97	0.97	0.85	0.85	0.85
NGC 4501	0.90	0.82	0.86	0.86	0.74	0.82	0.87
NGC 4535	0.89	0.85	0.91	0.92	0.85	0.87	0.87
NGC 4548	0.68	-0.44	0.67	0.74	0.07	0.69	0.72
NGC 4579	0.99	0.97	0.96	0.94	0.84	0.83	0.83
NGC 4725	0.82	0.72	0.77	0.76	0.44	0.64	0.78
NGC 5055	0.97	0.97	0.98	0.98	0.92	0.93	0.92
NGC 5236	0.97	0.89	0.89	0.88	0.81	0.81	0.80
NGC 5364	0.87	0.47	0.46	0.41	0.71	0.75	0.79
NGC 5457	0.90	0.80	0.89	0.90	0.21	0.38	0.50
NGC 7793	0.80	0.78	0.84	0.91	0.62	0.69	0.80

For most galaxies, though, the selection of the star formation tracer does not affect the analysis in Section 5. Given these results, we will proceed with using the extinction-corrected Hα data as the primary star formation tracer when comparing to the 3.6 μm emission. However, we will still use the 24 μm data as a star formation tracer in the cases where Hα data are not available, and we will also note any cases where the choice of star formation tracer would affect the identification of the heating source.

APPENDIX B: TESTS ON THE REMOVAL OF STELLAR EMISSION FROM THE 24 μm BAND

To tests the effects of removing the stellar photospheric emission from the 24 μm band, we applied the correction

$$I_\nu(24\ \mu m\ (\text{corrected})) = I_\nu(24\ \mu m\ (\text{observed})) - 0.032 I_\nu(3.6\ \mu m), \quad \text{(B1)}$$

from Helou et al. (2004). As we are primarily focused on how the logarithm of the 24 μm emission relates to the logarithms of the 160/250 and 250/350 μm surface brightness ratios in our primary analysis, we will focus on how the logarithm of the 24 μm changes when the correction is applied. We selected data from the 24 arcsec bins within the optical discs of the galaxies which met the criteria for the analysis on the 250/350 μm ratio in Section 5.

Statistics on comparisons of the 24 μm data with and without the correction are given in Table B1. The corrections have up to a 5 per cent effect on most of the 24 μm surface brightnesses. In a few situations, though, the corrections are significantly stronger. The most notable cases are the centres of NGC 3031 and 4725, where the 24 μm surface brightnesses change by up to 25 per cent. However, our analysis is more strongly affected by the logarithms of the 24 μm surface brightnesses, and these values do not change significantly. In the case of NGC 3031, the maximum change in the logarithm of the surface brightness is 2.5 per cent, in the case of NGC 4725, it is 1.2 per cent, and for all other galaxies, it is <1 per cent. Moreover, the logarithms of the 24 μm surface brightnesses with and without the corrections are very well correlated; the weighted correlation

Table B1. Statistics from tests of subtracting stellar continuum from 24 μm data.

Galaxy	Change in $I_\nu(24\ \mu m)$		Change in $\log(I_\nu(24\ \mu m))$	
	Median	Max	Median	Max
NGC 628	0.8 per cent	2.2 per cent	0.1 per cent	0.2 per cent
NGC 925	1.1 per cent	3.9 per cent	0.1 per cent	0.3 per cent
NGC 2403	1.1 per cent	5.0 per cent	0.1 per cent	0.4 per cent
NGC 3031	4.0 per cent	22.0 per cent	0.3 per cent	2.3 per cent
NGC 3184	1.2 per cent	2.2 per cent	0.1 per cent	0.2 per cent
NGC 3621	0.9 per cent	2.3 per cent	0.1 per cent	0.2 per cent
NGC 3631	0.7 per cent	1.4 per cent	0.1 per cent	0.1 per cent
NGC 3938	0.9 per cent	2.1 per cent	0.1 per cent	0.2 per cent
NGC 3953	1.5 per cent	6.3 per cent	0.1 per cent	0.6 per cent
NGC 4254	0.5 per cent	1.2 per cent	0.1 per cent	0.1 per cent
NGC 4303	0.8 per cent	2.5 per cent	0.1 per cent	0.2 per cent
NGC 4321	1.0 per cent	3.0 per cent	0.1 per cent	0.2 per cent
NGC 4501	1.7 per cent	4.5 per cent	0.2 per cent	0.4 per cent
NGC 4535	1.1 per cent	1.9 per cent	0.1 per cent	0.2 per cent
NGC 4548	2.6 per cent	8.1 per cent	0.2 per cent	0.8 per cent
NGC 4579	3.2 per cent	7.2 per cent	0.3 per cent	0.6 per cent
NGC 4725	2.7 per cent	13.4 per cent	0.2 per cent	1.2 per cent
NGC 4736	2.7 per cent	4.9 per cent	0.3 per cent	0.4 per cent
NGC 5055	1.3 per cent	2.7 per cent	0.1 per cent	0.2 per cent
NGC 5236	0.7 per cent	2.5 per cent	0.1 per cent	0.2 per cent
NGC 5364	1.3 per cent	3.8 per cent	0.1 per cent	0.3 per cent
NGC 5457	1.0 per cent	3.6 per cent	0.1 per cent	0.3 per cent
NGC 6946	0.7 per cent	2.6 per cent	0.1 per cent	0.2 per cent
NGC 7793	1.2 per cent	3.7 per cent	0.1 per cent	0.3 per cent

coefficients for the relations are equivalent to 1.00 to two decimal places.

Given these results, subtracting the stellar continuum emission from the 24 μm band is not critical for our analysis. In NGC 3031 and NGC 4725, where the corrections have a significant effect, we already mention in Section 3.2 that the 24 μm emission includes stellar emission that could affect its relation to the 160/250 and 250/350 μm ratios. In other galaxies, the effects of stellar emission on the 24 μm is minor or even negligible. We also have the issue that the 3.6 μm data may also include emission from hot dust associated with star formation (Lu et al. 2003; Mentuch et al. 2009, 2010), and while the analysis in Appendix C suggests that the effects of this hot dust are minimal, it does complicate the stellar continuum subtraction. We will therefore use the 24 μm data without applying the correction given by equation (B1).

APPENDIX C: COMPARISONS OF 1.6 AND 3.6 μm EMISSION

As stated in Section 3.3, mid-infrared data from the 1.6–3.6 μm range will generally trace starlight from the Rayleigh–Jeans side of the stellar SED. However, shorter wavelengths will be more strongly affected by dust extinction than longer wavelengths, while longer wavebands might include emission from hot dust. Therefore, we may expect to see minor variations in the shape of the 1.6–3.6 μm SED that could potentially affect the relation between near-infrared emission and the 160/250 or 250/350 μm ratios.

To investigate how the use of different near-infrared data may affect our results, we examined the relations between the logarithms of the 1.6 and 3.6 μm surface brightnesses for all galaxies in our sample. We used data from 24 arcsec bins within the optical discs of the galaxies that met the criteria for the analysis on the 250/350 μm surface brightness ratios in Section 5.

We found a very strong correlation between the 1.6 and 3.6 μm surface brightnesses. The weighted correlation coefficients for all of these relations are ∼1.00; the lowest value is 0.987 for NGC 5457 and 6946. This indicates that swapping one waveband for the other in the analyses in Sections 5 and 6 should have a minimal impact on the results. Table C1 gives data showing the mean fractional change in the $\log(I_\nu(1.6\,\mu\mathrm{m}))/\log(I_\nu(3.6\,\mu\mathrm{m}))$ over the full range of $\log(I_\nu(3.6\,\mu\mathrm{m}))$, which was found by fitting a line to the two quantities. The variations in the $\log(1.6\,\mu\mathrm{m})/\log(3.6\,\mu\mathrm{m})$ ratio are typically <5 per cent, which suggests that we will not see any major differences related to near-infrared colour variations if we use one of these wavebands instead of the other. It is very likely that the systematic variations that we do see in the $\log(1.6\,\mu\mathrm{m})/\log(3.6\,\mu\mathrm{m})$ ratio are caused by background artefacts, usually in the 2MASS 1.6 μm image, where often we spot alternating dark and bright rectangular regions. Fig. C1 shows NGC 925 as an example in which the low surface brightness structure in the 1.6 μm image appears much more asymmetrical than the background in the 3.6 μm image, probably because the background was oversubtracted in a data frame covering the south-east side of the galaxy.

Aside from these background artefacts, we detect only a small number of high signal-to-noise sources where the $\log(1.6\,\mu\mathrm{m})/\log(3.6\,\mu\mathrm{m})$ ratios deviate significantly (more than 0.2) from the mean values found in each galaxy. These are typically bright star-forming regions, such as the brightest star-forming region in NGC 2403, one of the bright regions in NGC 5457, and a few of the regions in NGC 6946. Some of the galactic nuclei with strong star formation activity, such as the nuclei of NGC 5236 and NGC 6946, have ratios that are suppressed relative to the rest of the data from the galaxies. In these situations, it is possible that we are either seeing higher-than-average dust attenuation that is reddening the stellar emission or we are seeing significant hot dust emission in the 3.6 μm bands, as suggested by Mentuch et al. (2009, 2010).

Table C1. Data from comparison of 1.6 and 3.6 μm emission.

Galaxy	Mean fractional change in $\log(I_\nu(1.6\,\mu\mathrm{m}))/\log(I_\nu(3.6\,\mu\mathrm{m}))$ over full range of $\log(I_\nu(3.6\,\mu\mathrm{m}))$
NGC 628	−0.036 ± 0.003
NGC 925	0.003 ± 0.019
NGC 1097	0.001 ± 0.001
NGC 2403	−0.039 ± 0.003
NGC 3031	−0.033 ± 0.001
NGC 3184	−0.035 ± 0.004
NGC 3351	−0.025 ± 0.006
NGC 3621	−0.014 ± 0.002
NGC 3631	−0.009 ± 0.003
NGC 3938	−0.043 ± 0.006
NGC 3953	−0.036 ± 0.004
NGC 4254	−0.029 ± 0.002
NGC 4303	−0.026 ± 0.011
NGC 4321	−0.015 ± 0.002
NGC 4501	−0.031 ± 0.002
NGC 4535	−0.040 ± 0.007
NGC 4548	−0.020 ± 0.001
NGC 4579	−0.014 ± 0.002
NGC 4725	−0.010 ± 0.001
NGC 4736	−0.033 ± 0.001
NGC 5055	−0.021 ± 0.001
NGC 5236	−0.005 ± 0.001
NGC 5364	−0.044 ± 0.016
NGC 5457	−0.026 ± 0.003
NGC 6946	0.013 ± 0.002
NGC 7793	−0.032 ± 0.003

Overall, though, we simply do not see many regions where the near-infrared colours look significantly redder than average. This may be because we are averaging over relatively large areas [areas that are four times larger than what Mentuch et al. (2010) used]. Reddening caused by extinction or hot dust emission in extreme environments may be diluted by regions with more typical colours. Given these results, we feel confident that the 3.6 μm data in our analysis are generally unaffected by hot dust emission, although we do acknowledge that we may encounter some problems with a few extreme cases. Moreover, it is more advantageous to use the 3.6 μm images because of the superior signal-to-noise and better background subtraction in the 3.6 μm images. We therefore rely on the 3.6 μm band as a tracer of emission from the evolved stellar population in our analysis.

APPENDIX D: TESTS OF THE REMOVAL OF EMISSION FROM STAR-FORMING REGIONS FROM THE 3.6 μm BAND

It would potentially be desirable to treat the 3.6 μm band as a tracer of the intermediate-aged and older stellar population by removing the contributing emission from star-forming regions. To derive such a correction, we used the Starburst99 model version 6.0.3 (Leitherer et al. 1999)[10] to model the Hα and 3.6 μm from stars formed either

[10] Accessed at http://www.stsci.edu/science/starburst99/docs/default.htm

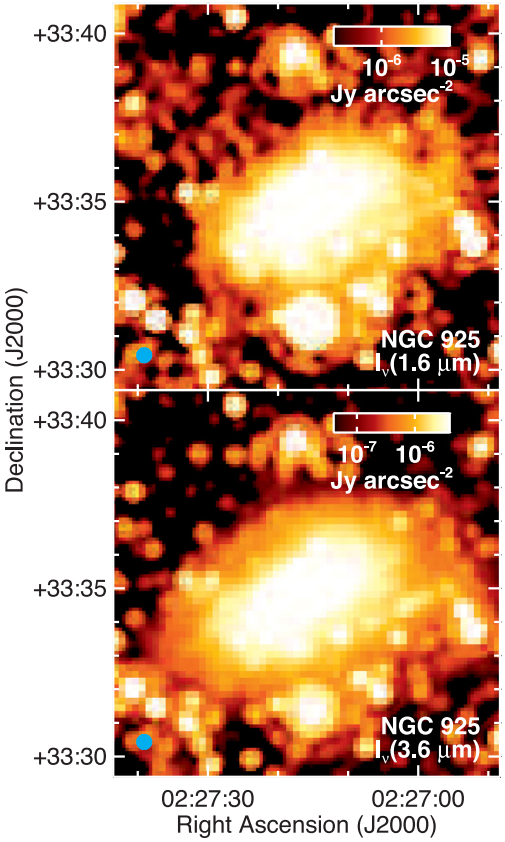

Figure C1. Example 1.6 and 3.6 μm images of NGC 925, with the colour scale adjusted to show the differences in the radial profiles of the observed 1.6 and 3.6 μm emission as well as low-level background artefacts in the 1.6 μm map. The PSFs of the data have been matched to the PSF of the 350 μm data, which has an FWHM of 25 arcsec. The cyan circles in each panel show the size of the PSF.

in an instantaneous burst of star formation or in continuous star formation. We used a Kroupa initial mass function with $\Phi(M) \propto M^{2.3}$ for stars with masses >0.5 $M_\odot$ and $\Phi(M) \propto M^{1.3}$ for stars with masses <0.5 $M_\odot$ (Kroupa 2001). We performed simulations only for solar metallicities (which should approximate the metallicities of the spiral galaxies in our sample) and used all other default settings for the models. As Starburst99 does not calculate flux densities in the IRAC bands, we derived these values by following the instructions given in the Spitzer Data Analysis Cookbook (Spitzer Science User Support and Instrument Teams and IRSA Science User Support Team 2012)[11].

The 3.6 μm/Hα ratios from the Starburst99 simulation are plotted in Fig. D1. In the first 3 Myr after an instantaneous burst of star formation or after the onset of continuous star formation, the ratio of the 3.6 μm flux density to Hα flux stays at $(2.7 \pm 0.2) \times 10^8$ Jy (erg s^{-1} cm^{-2})$^{-1}$ regardless of which star formation scenario is used. After 3 Myr, photoionizing stars evolve off of the main sequence, and the 3.6 μm/Hα ratio changes notably, although how it changes depends on which star formation scenario we use. In an instantaneous burst, the Hα emission drops off significantly after 3 Myr, and the 3.6 μm/Hα ratio increases exponentially to $\sim 8.5 \times 10^{10}$ Jy (erg s^{-1} cm^{-2})$^{-1}$. However, it is unclear that we would detect

[11] http://irsa.ipac.caltech.edu/data/SPITZER/docs/dataanalysistools/cookbook/

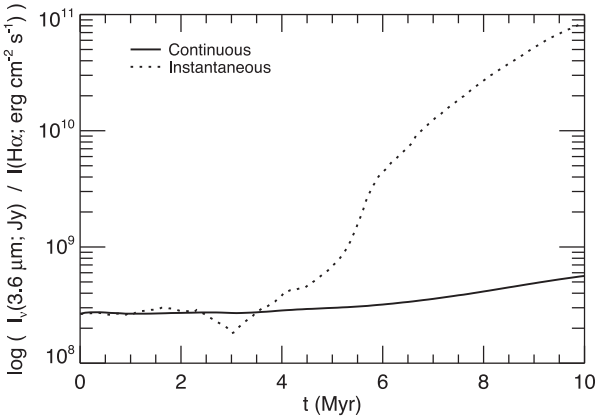

Figure D1. Plot of the 3.6 μm to Hα surface brightness ratio as a function of time since the onset of star formation as determined using Starburst99. The solid line represents the continuous star formation scenario, while the dotted line represents the instantaneous burst scenario.

Hα emission from stellar populations much older than 3 Myr, and if we did, then it would seem unlikely that such stellar populations would produce a significant fraction of the total Hα emission. In the continuous star formation scenario, the ratio rises upwards more gradually, increasing to $\sim 5.7 \times 10^8$ Jy (erg s^{-1} cm^{-2})$^{-1}$ at 10 Myr. While the entire stellar population of a spiral galaxy may be treated as undergoing continuous star formation, it may be more appropriate to treat individual regions as instantaneous bursts of star formation. We will therefore assume that the Hα emission that we are observing originates mainly from stars that formed in the past 3 Myr, in which case, we will apply 2.7×10^8 Jy (erg s^{-1} cm^{-2})$^{-1}$ to the Hα fluxes to estimate the 3.6 μm emission from stars that have formed in the past 3 Myr.

We examined how the corrections affected the 3.6 μm surface brightness itself as well as the logarithm of the 3.6 μm surface brightnesses in galaxies for which we had Hα data. The corrections were derived from the extinction-corrected Hα intensities calculated using equation (1). We used the same 24 arcsec binned data that were used for the analysis on the 250/350 μm surface brightness ratio in Section 5. The data are shown in Table D1.

As can be seen by these tests, the correction generally has a very minor impact on the 3.6 μm emission. In most cases, the correction is <2 per cent, indicating that >98 per cent of the total 3.6 μm emission from all regions within the optical discs comes from non-ionizing intermediate-aged and evolved stars. We did see some stronger changes in a few individual star-forming regions. In NGC 5471, which is a location containing a bright H II region in the outer disc of NGC 5457, we estimate that 17 per cent of the 3.6 μm emission may originate from stars with ages <3 Myr. In a few other star-forming regions at the periphery of the disc of NGC 5457 and a couple of star-forming regions in NGC 925, 2403, 3621, 3938, 4535, and 7793, the correction changed the 3.6 μm emission by 2–7 per cent. However, these few 'extreme' cases have a <1 per cent effect on the logarithm of the 3.6 μm emission, which we use in most of our analysis. Moreover, the weighted correlation coefficient between the logarithms of the uncorrected and corrected 3.6 μm surface brightnesses is 1.00 in all cases.

The relatively small effect of this adjustment to the 3.6 μm data ultimately has no significant effect on our analysis. If we attempted to account for stars older than 3 Myr, then the changes in the 3.6 μm emission would be higher, but this would depend upon being able to determine what the star formation history is for these regions.

Table D1. Statistics from tests of subtracting emission from stars with ages <3 Myr from 3.6 μm emission.

Galaxy	Change in I_ν(3.6 μm)		Change in log(I_ν(3.6 μm))	
	Median	Max	Median	Max
NGC 628	0.4 per cent	1.3 per cent	0.0 per cent	0.1 per cent
NGC 925	0.9 per cent	4.4 per cent	0.1 per cent	0.3 per cent
NGC 2403	0.7 per cent	6.8 per cent	0.1 per cent	0.6 per cent
NGC 3031	0.2 per cent	1.6 per cent	0.0 per cent	0.1 per cent
NGC 3184	0.5 per cent	1.1 per cent	0.0 per cent	0.1 per cent
NGC 3621	0.7 per cent	4.1 per cent	0.1 per cent	0.3 per cent
NGC 3631	0.9 per cent	1.5 per cent	0.1 per cent	0.1 per cent
NGC 3938	0.5 per cent	2.8 per cent	0.0 per cent	0.2 per cent
NGC 3953	0.2 per cent	0.7 per cent	0.0 per cent	0.1 per cent
NGC 4254	0.9 per cent	1.7 per cent	0.1 per cent	0.1 per cent
NGC 4303	0.6 per cent	1.6 per cent	0.1 per cent	0.2 per cent
NGC 4321	0.5 per cent	1.1 per cent	0.0 per cent	0.1 per cent
NGC 4501	0.3 per cent	0.5 per cent	0.0 per cent	0.0 per cent
NGC 4535	0.6 per cent	2.2 per cent	0.1 per cent	0.2 per cent
NGC 4548	0.1 per cent	0.2 per cent	0.0 per cent	0.0 per cent
NGC 4579	0.2 per cent	0.4 per cent	0.0 per cent	0.0 per cent
NGC 4725	0.2 per cent	0.5 per cent	0.0 per cent	0.0 per cent
NGC 5055	0.3 per cent	0.7 per cent	0.0 per cent	0.1 per cent
NGC 5236	0.5 per cent	2.0 per cent	0.0 per cent	0.2 per cent
NGC 5364	0.4 per cent	1.5 per cent	0.0 per cent	0.1 per cent
NGC 5457	0.4 per cent	17.0 per cent	0.0 per cent	1.4 per cent
NGC 7793	0.8 per cent	4.0 per cent	0.1 per cent	0.3 per cent

For reference, we estimate using the physical dimensions of the 24 arcsec resolution elements in Table 1 and assuming a rotational velocity of 200 km s^{-1} that stars may pass through the resolution elements on periods ranging from 2 to 12 Myr. In some cases, the correction for the 3.6 μm band that we are already using (which assumes that the stellar populations are <3 Myr in age) is already applicable. For older regions, we would need to guess the star formation history of the regions. We also have the complicating issue that the star formation tracers that we are using are imperfect for estimating this correction. The Hα emission without the extinction correction would give a correction to the 3.6 μm band that is too low, while the Hα emission combined with the 24 μm band may potentially be affected by 24 μm emission from diffuse dust heated by the ISRF (see Appendix A). These issues along with the relatively minor benefit from removing the emission from young stars from the 3.6 μm band lead us to the conclusion that we should simply use the 3.6 μm surface brightnesses as observed for our analysis.

APPENDIX E: OFFSETS BETWEEN ENHANCED INFRARED SURFACE BRIGHTNESS RATIOS AND SPIRAL ARMS

As stated in Section 4, we see small offsets between the star-forming regions and the colour temperatures in some of the images in Fig. 1. This phenomenon had been seen previously. Bendo et al. (2012a) and Foyle et al. (2012) illustrated that regions with enhanced colour temperatures in the spiral arms of M83 appeared offset from the star-forming regions, and Mentuch Cooper et al. (2012) had indicated that such an offset also appeared to be present in M51 but did not illustrate this offset. To examine this further, we measured the profiles of surface brightnesses across spiral arm segments in NGC 5236 and 6946, the two closest galaxies where we see this phenomenon. Fig. E1 shows the locations where we measured the profiles in these galaxies, and Fig. E2 shows the profiles themselves.

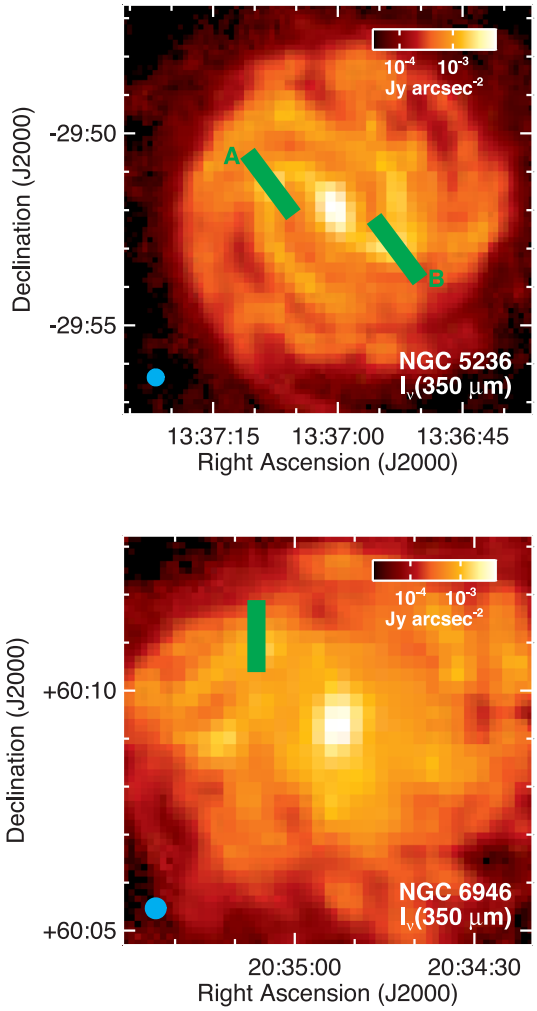

Figure E1. The 350 μm images for NGC 5236 and 6946 with green lines indicating locations where surface brightness profiles were measured across the spiral arms. The cyan circles show the FWHM of the PSF. The profiles themselves are shown in Fig. E2.

These images illustrate similar structures in all three spiral arm segments. The 350 μm data serve as a proxy for the dust mass, as the band lies in a regime of the SED where it is relatively insensitive to the temperature variations seen in these data. We will refer to the peak of the 350 μm emission as the dust lane within these galaxies. The Hα emission, which traces gas photoionized by star-forming regions, and the 24 μm emission, which traces hot dust heated by the star-forming regions, peak to one side of the 350 μm emission, although the difference between the peaks is small compared to the 25 arcsec resolution of the data. None the less, this would be consistent with the classical depiction of spiral density waves in which gas falls into the wave, gets compressed, and forms stars on the other side of the wave (e.g. Roberts 1969; Elmegreen 1979). In the line segments we have selected, material is flowing into the concave sides of the spiral density waves, and new stars are found on the convex side. The asymmetric distribution of dust and young stars around the star-forming regions has a few potential effects on dust heating in these locations.

First, we can see in the NGC 5236 data that the Hα emission is offset relative to the 24 μm emission, although this offset is small compared to the 25 arcsec resolution of the data. This will occur in part because the star-forming regions closer to the dust lane are

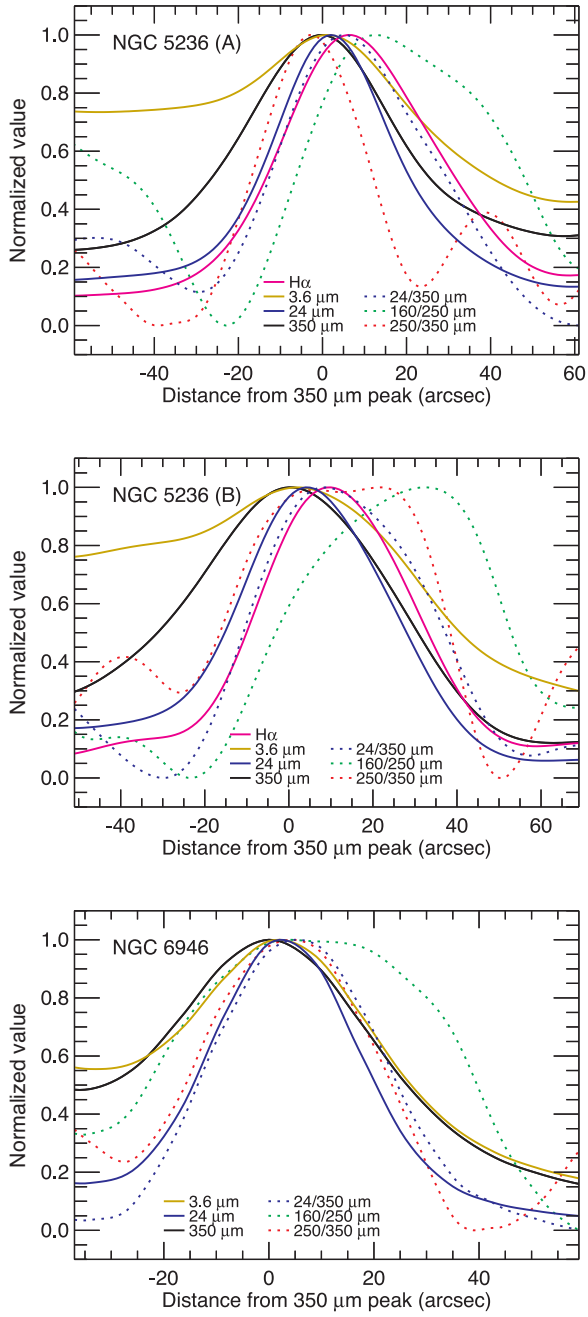

Figure E2. Profiles of the surface brightnesses (shown as solid lines and normalized so that the peaks equal 1) and surface brightness ratios (shown as dotted lines and normalized so that the profiles range from 0 to 1) across spiral arms in NGC 5236 and 6946. The locations of these profiles are shown in Fig. E1. Measurements were made at 1 arcsec intervals in 24-arcsec-wide regions in data where the PSF FWHM is 25 arcsec. The *x*-axes show the distance from the peak in the 350 μm profile, with positive *x*-values showing distance from the 350 μm peak on the downstream side of the arms. The uncertainties for the normalized surface brightness profiles are $\lesssim$0.01, and the uncertainties for the normalized surface brightness ratios are ∼0.10.

more obscured, leading to a change in the Hα/24 μm ratio. The normalized Hα emission is also higher than the normalized 24 μm emission at locations downstream from the spiral arms. Some fraction of this Hα emission may originate from gas in the diffuse ISM photoionized by photons escaping from star-forming regions. This enhancement in Hα emission would be seen on only one side of the star-forming regions because the optical depth is much higher on the other side of the regions, which means that photoionizing photons can travel much further away from the dust lane than towards it.

From the perspective of our analysis, the most interesting feature here is the presence of the strongly enhanced 160/250 μm ratio on the opposite side of the star-forming regions from the dust lane, which can be offset by a distance comparable to the 25 arcsec resolution of the data. The ratio is clearly not tracing the temperature of dust heated locally by the star-forming regions; otherwise, the 160/250 μm ratio would peak at the same location as the 24/350 μm ratio. A similar offset in enhanced PAH emission in the IRAC 8 μm band was found in M83 by Jones et al. (in preparation). They even found that the 8/250 μm surface brightness ratio (a measure of PAH excitation normalized by dust mass) was correlated with the 160/250 μm ratio, suggesting that both the dust emission at 160 μm and the PAH excitation were linked.

The peak in the 160/250 μm ratio may be offset for one of two reasons. First, the 160 μm emission from these galaxies may primarily originate from dust heated by photoionizing light escaping the star-forming regions into the diffuse ISM. Because the light primarily propagates away from the dust lanes, the peak in the 160/250 μm ratio appears offset. The physical distance between the peak in the 160/250 μm ratios and the peak in the 350 μm emission is ∼0.5 kpc. This distance is in the middle of the 0.1–1 kpc range of the mean free path of *V*-band photons in galaxies given by the analysis from Xilouris et al. (1999) and Bianchi (2007), which implies that the 160 μm emission could be from dust heated by diffuse light from star-forming regions. The other possibility is that emission in the 160 μm band is from dust in an optically thin environment heated locally by B and A stars that have emerged from the dusty star-forming regions 10–100 Myr ago. These stars would not produce the photons needed to photoionize hydrogen but would produce substantially strong radiation fields that include large numbers of soft ultraviolet photons that could warm up the large dust grains.

The 250/350 μm ratio presents relatively different results in the three profiles. In profile A in NGC 5236, the ratio peaks on the side of the dust lane opposite the side of the star-forming region, and in NGC 6946, the peak corresponds to the location of the peak in the 3.6 μm emission. This would be consistent with the 250/350 μm ratio tracing the temperature of the dust in the spiral arm that is shielded from the star-forming regions and heated by the radiation field from the evolved stellar population. In profile B in NGC 5236, the 250/350 μm ratio peaks in two locations: one peak corresponds to the location of the 24 μm peak, while the other appears ∼15 arcsec further downstream in a location where the 160/250 μm ratio is also enhanced. This could indicate that the ratio in this location is still sensitive to heating by either light diffusing from the star-forming regions or unobscured B and A stars. However, the structures in the 250/350 μm ratio map for NGC 5236 are relatively poorly defined overall and might be affected by residual striping in the 350 μm data, so it is difficult to interpret the significance of the 250/350 μm profiles for the galaxy.

As we stated earlier, NGC 5236 and 6946 are the two galaxies in our sample where we see these structures most prominently. We do see some hints of similar structures in the northern part of NGC 628, but the effect is not particularly strong. Aside from these galaxies, though, we do not see any cases where we can see significant offsets between the spiral arm structures traced by the 24 μm emission and the structures traced by the 160/250 and 250/350 μm ratios. The structures appear on scales of $\lesssim$0.5 kpc, so for galaxies at $\gtrsim$5 Mpc, offsets between the surface brightness ratios and the star-forming regions may not be readily apparent within data

Table F1. Weighted correlation coefficients for relations between 160/250 and 250/350 μm ratios and tracers of heating sources in data with different bin sizes.

Galaxy	Bin size (arcsec)	Weighted correlation coefficients			
		$\log(I_\nu(160\,\mu m)/I_\nu(250\,\mu m))$ versus $\log(I(H\alpha))^a$	$\log(I_\nu(160\,\mu m)/I_\nu(250\,\mu m))$ versus $\log(I_\nu(3.6\,\mu m))$	$\log(I_\nu(250\,\mu m)/I_\nu(350\,\mu m))$ versus $\log(I(H\alpha))^a$	$\log(I_\nu(250\,\mu m)/I_\nu(350\,\mu m))$ versus $\log(I_\nu(3.6\,\mu m))$
NGC 3031	24	0.17	0.84	0.16	0.87
	120	−0.07	0.91	0.17	0.90
NGC 5457	24	0.89	0.57	0.40	0.89
	120	0.92	0.57	0.53	0.94

Note: [a]The Hα data used here were corrected for extinction using 24 μm data.

at 25 arcsec resolutions. The remaining galaxies within 5 Mpc may not exhibit these structures for a large number of reasons. In NGC 3031, the 160/250 and 250/350 μm ratios appear more strongly influenced by the evolved stellar population, so we would not expect to see this phenomenon at all. Meanwhile, NGC 2403 and 7793 are both flocculent galaxies where, because these two galaxies lack the large shock fronts created by the spiral density waves, star formation is expected to occur in clouds that collapse because of local gravitational instabilities. Dust may be distributed symmetrically around star-forming regions in these galaxies, and simulations by Dobbs & Pringle (2010) suggest that no stellar age gradients will be seen across the spiral segments. In the scenario where the 160/250 or 250/350 μm ratios are enhanced by light diffusing from star-forming regions, the light would diffuse symmetrically around star-forming regions. In the scenario where the ratios are enhanced by B and A stars, it may be possible that the B and A stars are not located preferentially on one side of current star formation sites. In either case, the 160/250 and 250/350 μm ratios will peak in the same locations as the emission from the star-forming regions themselves (if the star-forming regions influence the ratios).

We recommend treating these results cautiously. Although the offsets in the peaks of the surface brightness ratio profiles are quite apparent, the offsets among individual wavebands are relatively small compared to the 25 arcsec FWHM of the PSF. Unidentified astrometry problems could produce some of the patterns seen in these profiles, although we have checked the astrometry of these data using foreground stars and background galaxies outside the optical discs of the galaxies, and the structures in the profiles continue to appear even when small adjustments are made to the astrometry of the data (or adjustments are not applied). It is unlikely that the PSF-matching steps could have introduced some structures. This step should match not only the FWHMs of the PSFs but also the profiles of the PSFs, and the kernels from Aniano et al. (2011) that we used are based on observational data and should contain features related to the instrument and data processing. Even though these kernels do not always work perfectly, the artefacts from this process that appear around bright sources in the colour temperature maps usually look symmetric, whereas the structures that we see associated with the spiral arms in the 160/250 μm maps are asymmetric. It is more likely that the offset 160/250 μm features are intrinsic structures within the galaxies rather than artefacts related to astrometry or PSF-matching issues.

APPENDIX F: TESTS OF RESOLUTION EFFECTS ON THE DATA

Because the galaxies are located at distances that vary by a factor of 7 and also because the same analytical methods have been applied to the same galaxies using data at different resolutions, we tested the effects of performing our analyses using data measured in different sized bins. For this analysis, we selected NGC 3031 and 5457, the two galaxies with the largest angular sizes in the sample. We rebinned the data for these galaxies into 120 arcsec bins. This is equivalent to shifting NGC 3031 from 3.6 to 18.0 Mpc and to shifting NGC 5457 from 6.7 to 33.5 Mpc, which are equivalent to or larger than the distances for the furthest galaxies in our sample. We then repeated the analysis in Sections 5 and 6.

Table F2. Results from fitting equation (2) to the 160/250 and 250/350 μm surface brightness ratios.

Galaxy	Bin size (arcsec)	η	
		160/250 μm	250/350 μm
NGC 3031	24	0.79 ± 0.02	0.95 ± 0.03
	120	0.72 ± 0.11	0.73 ± 0.17
NGC 5457	24	0.37 ± 0.01	1.00^a
	120	0.21 ± 0.05	1.00^a

Note: [a]For these fits, I(SFR) in equation (2) was found to be negligible compared to $A_1 I_\nu(3.6\,\mu m)$. We therefore fit $\ln(I_\nu(250\,\mu m)/I_\nu(350\,\mu m))$ to $\ln(I_\nu(3.6\,\mu m))$ using a linear function.

Table F1 shows the changes in the correlation coefficients in the relations between the infrared surface brightness ratios and the tracers of different dust heating sources. We generally see the correlation coefficients increase up to 0.15 when we use the larger bin size except in the relation of the 160/250 μm ratio to Hα emission, where the relation exhibited uncorrelated scatter in both the 24 and 120 arcsec binned data. We also still generally obtain the same results for these two galaxies that we did in Section 5. Regardless of the bin size used, the 160/250 and 250/350 μm ratios for NGC 3031 and the 250/350 μm ratios for NGC 5457 appear much better correlated with the 3.6 μm surface brightness, while the 160/250 μm ratios for NGC 5457 still appear better correlated with the Hα emission.

Table F2 shows the resulting η after applying the decomposition analysis in Section 6 to data with different bin sizes. Except for the η(250/350 μm) for NGC 5457, where the I(SFR) term was negligible, the resulting η all decrease. The decrease in η(160/250 μm) for NGC 3031 is relatively small compared to the uncertainties in the η values for the 120 arcsec bins. The η(250/350 μm) is 0.22, although this is comparable to the uncertainty in the methodology following the analysis in Appendix G (0.15) as well as the uncertainty of 0.17 in η(250/350 μm) for the 120 arcsec binned data that was determined using the Monte Carlo analysis. The η(160/250 μm) for NGC 5457 decreases by 0.16, which is also approximately equivalent to the uncertainty of 0.15 in the methodology. The change may have resulted from combining brighter emission from warmer dust heated locally by star-forming regions with fainter emission

from cooler dust heated by older stars. The dust emission observed in these coarser bins would appear to be dominated more by dust heated by star-forming regions, an issue also highlighted by Galliano et al. (2011).

In summary, these tests represent the most severe tests of resolution and distance-related effects that could affect the data. The analysis of the correlation between surface brightness ratios and dust heating sources in Section 5 should be robust against distance-related effects. The decomposition analysis in Section 6 is somewhat affected by distance-related effects, although the changes in the derived η values are generally consistent when taking into account both the 0.15 uncertainty in the methodology and the uncertainties from the Monte Carlo analysis. These issues are noted in Section 6, but we will treat the η as though resolution and distance have a minor effect on the data.

APPENDIX G: TESTS OF MEASURING η USING SIMULATED DATA

To test the effectiveness of using equations (2) and (3) to derive the relative fraction of variation in emission in a waveband that is related to heating by a specific population of stars, we created simplified models of dust heating within disc galaxies. The dust grains are treated as modified blackbodies where $E \propto T^6$, which is appropriate for $\beta = 2$. We assume that the dust is at thermodynamic equilibrium with the local radiation field and that the temperature depends upon heating from two stellar populations; this effectively excludes stochastically heated dust as well as more complex radiative transfer effects. The distribution of dust mass is treated as arbitrary.

To represent the dust heated by the two different stellar populations, we created two circular discs with diameters of 10 arcmin and pixel sizes of 1 arcsec. For the energy E_{ES} from the evolved stellar population (including intermediate-aged and older stars), we used a smooth exponential disc with a scalelength of 150 arcsec. For the energy E_{SF} from the star-forming regions, we created a disc containing 150 randomly placed unresolved sources with amplitudes scaled by a radially-varying exponential function with a scalelength of 240 arcsec and five additional randomly placed sources that are set to two times the peak of the exponential profile. This is a simplified representation of the star-forming structures that could be expected in a flocculent spiral galaxy, and the broader scalelength for the star-forming regions compared to the evolved stellar populations reflects how star-forming regions are distributed more broadly than evolved stars in spiral galaxies. We assume that the distribution of both stellar populations and the dust perpendicular to the disc of the galaxy are similar and therefore do no additional computations for the vertical propagation of light.

The E functions were then rescaled to compute SEDs based on modified blackbodies with $E \propto T^6$. The energy-weighted mean T was set to 15 K for the evolved stellar population component and 25 K for the star-forming component, which is similar to the temperatures measured for the separate thermal components in Section 7.1. The data were then used to create maps with 1 arcsec pixels of the intensities from these components at 160, 250, and 350 μm. The maps were convolved with a 25 arcsec Gaussian function, which is similar to the PSF of the SPIRE 350 μm data. The maps were then rebinned into 24 arcsec bins for the quantitative analysis.

We examined data created for multiple scenarios where the E values were rescaled to create input η(250 μm) ratios ranging from 0.1 to 0.9. We then fit the 160/250 and 250/350 μm ratios using E_{ES} and E_{SF} in equation (2) and computed output η values for these ratios using equation (3), which we then compare to the input η measured at the shorter wavelength.

Table G1. Comparison of input and output η results.

Scenario number	Input η		Output η	
	160/250 μm	250/350 μm	160/250 μm	250/350 μm
1	0.11	0.10	0.13	0.12
2	0.19	0.20	0.18	0.19
3	0.26	0.30	0.22	0.25
4	0.33	0.40	0.26	0.32
5	0.41	0.50	0.31	0.40
6	0.49	0.60	0.37	0.49
7	0.58	0.70	0.46	0.61
8	0.69	0.80	0.58	0.73
9	0.82	0.90	0.75	0.86

Mean input and output η values from these tests are given in Table G1. Fig. G1 shows the model surface brightnesses for the star-forming and evolved stellar populations, the input η and 160 and 250 μm, the resulting 160/250 and 250/350 μm colour temperature maps, and the output η maps for the 160/250 and 250/350 μm ratios for scenario 5 [where the input η(250 μm) is set to 0.50].

The input and output maps agree within ∼1 K in most locations, but the brighter star-forming regions tend to be ∼5 K hotter in the output images than in the input images. This illustrates the limitations of using equation (2) to relate an observed colour temperature to emission from multiple dust heating sources, at least over large temperature ranges. The measured η in individual locations may be within 0.20 of the input value, but we typically measure a global mean η that is within 0.10 of the input value. We get input and output η values within 0.01 when $\eta \lesssim 0.20$. On the other hand, the difference between input and output η values is 0.10–0.15 in situations where η is between 0.50 and 0.70. The output η value is always lower than the input η value, which demonstrates that the methodology exhibits a systematic bias that could potentially be corrected to improve the accuracy of the measured η.

Given these results, we will use 0.15 as the uncertainties in the η values from the analysis in Section 6 when rescaling global flux densities to create SEDs for separate thermal components. However, we will point out that the uncertainties could be higher in multiple circumstances. If the difference between the dust temperatures is larger, then the assumptions behind equation (2) no longer apply and the uncertainty in η could increase. As mentioned elsewhere in the text, the uncertainty in η will be high if the star-forming regions and evolved stellar populations have similar distributions or if the mean free path of light heating the dust is larger than the resolution elements of our data.

Although we only show results for 160/250 and 250/350 μm ratios, we did find that the results may still be reliable when creating surface brightness ratios based on any two wavebands where the longer waveband samples emission on the Rayleigh–Jeans side of the SED. However, the η values could become more uncertain if both wavebands sample emission from the peak or Wein side of the dust SED. This should be taken into account when attempting to apply this methodology to other data sets.

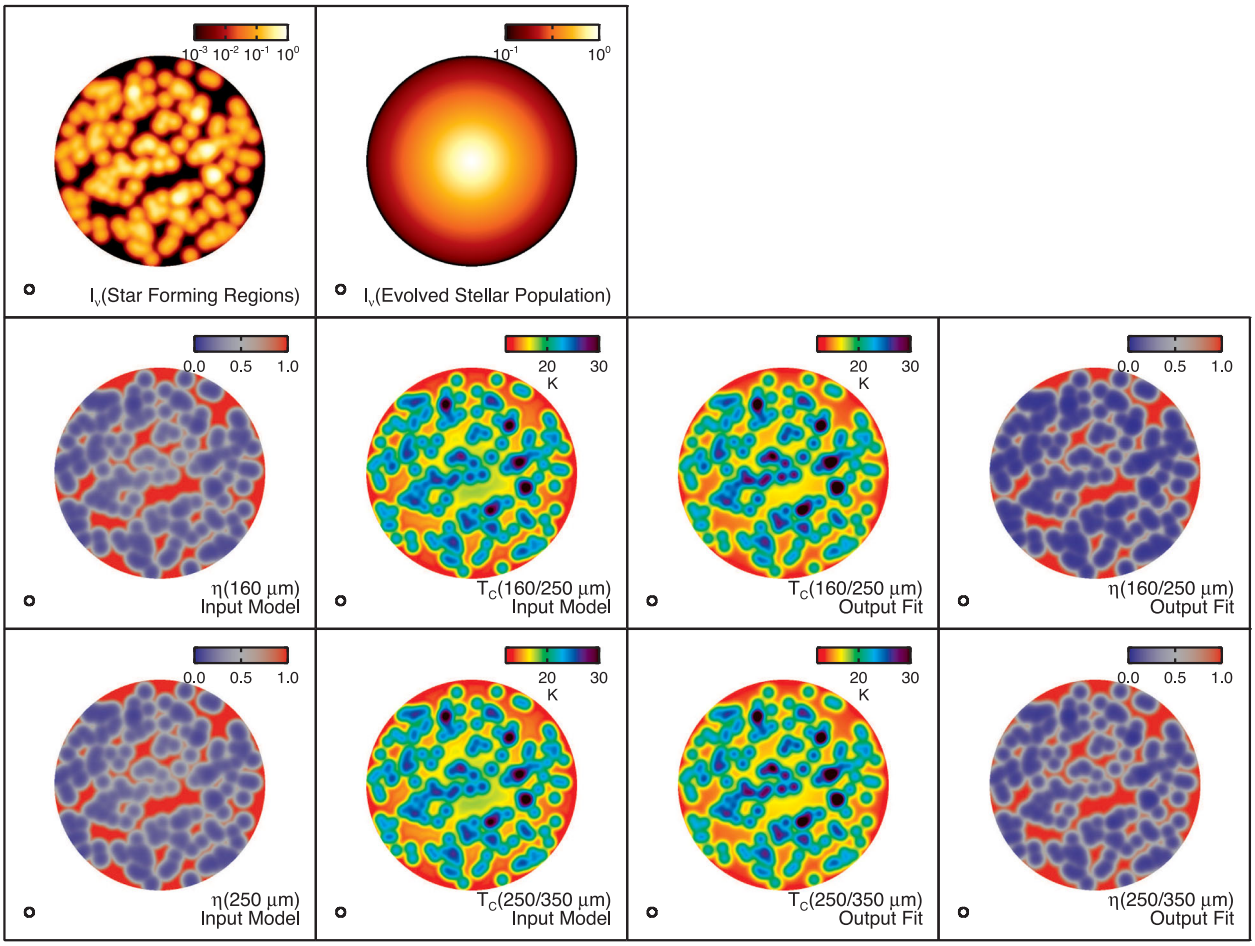

Figure G1. Input and output data for tests in Appendix G showing the effectiveness of using equations (2) and (3) and the methodology in Section 6 to measure the fraction of dust heated by different populations of stars by comparing the emission from the dust heating sources to the observed infrared surface brightness ratios. All data are for a simulated face-on galaxy disc where the emission is truncated at a diameter of 10 arcmin and where the resolution of the data is 25 arcsec. The top row shows the model surface brightnesses for star-forming and evolved stellar populations (with peak values normalized to one). The bottom two rows show, for scenario 5 in Table G1 [where the input $\eta(250\ \mu m)$ is set to 0.50], the input η and 160 and 250 μm, the resulting input 160/250 and 250/350 μm colour temperature maps, the best-fitting output colour temperature maps, and the output η maps for the 160/250 and 250/350 μm ratios. The colour temperature maps are computed using $\beta = 2$. The output $\eta(160/250\ \mu m)$ should be compared to the input $\eta(160\ \mu m)$, and the output $\eta(250/350\ \mu m)$ should be compared to the input $\eta(250\ \mu m)$.

SUPPORTING INFORMATION

Additional Supporting Information may be found in the online version of this article:

Figure 1. Hα, 3.6 μm, 160/250 μm, and 250/350 μm images of all sample galaxies.
Figure 7. Results from using equation (2) to fit the 160/250 and 250/350 μm surface brightness ratios as a function of both the Hα and 3.6 μm data. (http://mnras.oxfordjournals.org/lookup/suppl/doi:10.1093/mnras/stu1841/-/DC1).

Please note: Oxford University Press is not responsible for the content or functionality of any supporting materials supplied by the authors. Any queries (other than missing material) should be directed to the corresponding author for the article.

This paper has been typeset from a TEX/LATEX file prepared by the author.